Research Square

Preprints are preliminary reports that have not undergone peer review.
They should not be considered conclusive, used to inform clinical practice,
or referenced by the media as validated information.

Revealing an evolving corona around a prototypical intermediate-mass black hole

Samuzal Barua

samuzal.barua@gmail.com

Shanghai Astronomical Observatory, Chinese Academy of Sciences

Hengxiao Guo

Shanghai Astronomical Observatory

Andrew Fabian

University of Cambridge https://orcid.org/0000-0002-9378-4072

Zhen Yan

Shang Hai AO https://orcid.org/0000-0002-5385-9586

Minfeng Gu

Shanghai Astronomical Observatory

Unnanti Kashyap

Department of Physics and Astronomy, Texas Tech University, Lubbock, TX 79409-1051, USA

Federico Vincentelli

Coventry University

Wenwen Zuo

Shanghai Astronomical Observatory, Chinese Academy of Sciences

Jingbo Sun

Shanghai Astronomical Observatory, Chinese Academy of Sciences

Ian McHardy

University of Southampton

Edward Cackett

Wayne State University https://orcid.org/0000-0002-8294-9281

Joey Neilsen

Villanova University https://orcid.org/0000-0002-8247-786X

Guglielmo Mastroserio

Instituto Universitario di Studi Superiori di Pavia: Pavia, Lombardy, Italy

Alice Borghese

ICE https://orcid.org/0000-0001-8785-5922

Physical Sciences - Article

Keywords:

Posted Date: January 18th, 2026

DOI: https://doi.org/10.21203/rs.3.rs-8263435/v1

License: This work is licensed under a Creative Commons Attribution 4.0 International License.
Read Full License

Additional Declarations: There is **NO** Competing Interest.

Revealing an evolving corona around a prototypical intermediate-mass black hole

Samuzal Barua[1], Hengxiao Guo[1], Andrew C. Fabian[2], Zhen Yan[1], Minfeng Gu[1], Unnati Kashyap[3], Federico Vincentelli[4,5,6], Wenwen Zuo[1], Jingbo Sun[1], I. M. M^{c}Hardy[6], Edward M. Cackett[7], Joey Neilsen[8], Guglielmo Mastroserio[9], Alice Borghese[10]

[1]Shanghai Astronomical Observatory, Chinese Academy of Sciences, 80 Nandan Road, Shanghai, 200030, People's Republic of China.
[2]Institute of Astronomy, The University of Cambridge, Madingley Road, CB3 OHA, Cambridge, UK.
[3]Department of Physics and Astronomy, Texas Tech University, Lubbock, TX 79409-1051, USA.
[4]Fluid and Complex Systems Centre, Coventry University, CV1 5FB, UK.
[5] INAF–Istituto di Astrofisica e Planetologia Spaziali, Via del Fosso del Cavaliere 100, I-00133, Roma, Italy.
[6]School of Physics & Astronomy, University of Southampton, Southampton SO17 1BJ, UK.
[7]Wayne State University, Department of Physics & Astronomy, 666 W Hancock St, Detroit, MI 48201, USA.
[8]Villanova University, Department of Physics, Villanova, PA 19085, USA.
[9]Istituto Universitario di Studi Superiori di Pavia: Pavia, Lombardy, Italy.
[10]European Space Agency (ESA), European Space Astronomy Center (ESAC): Villafranca del Castillo, Madrid, Spain.

X-ray observations of accreting black holes reveal X-ray reverberation [1], which is an effective approach to infer the geometrical arrangement of the disc-corona system [2] and the dynamics of the inner accretion flow [3]. A promising scenario to explain rapid X-ray variations is that they are a consequence of both accretion rate and coronal height changes [4, 5]. While supermassive black holes (SMBHs) [e.g. 6–9] mostly, and a handful of stellar mass black holes (sBHs) [e.g. 10–13] show reverberation, it is not often seen in the intermediate-mass black hole (IMBH) regime due to the low count rate from the inner disc, except for a few low mass objects, $M_{\rm BH} < 3 \times 10^6\ M_\odot$, showing soft X-ray lags [14]. Here we examine the closest prototypical IMBH, NGC 4395, which has high X-ray flux variability, allowing it to be treated as an ideal proxy, in which iron-K reverberation lag is detected. We undertake two independent approaches in NGC 4395: X-ray reverberation and reflection spectroscopy [15] – which relies on the full treatment of general relativistic (GR) ray-tracing calculations. The combined result of these approaches reveals an evolving corona that changes height from $1.65^{+1.86}_{-0.75}\ R_{\rm g}$ ($= GM_{\rm BH}/c^2$) to $26.66^{+2.71}_{-4.77}\ R_{\rm g}$ with increasing luminosity. GR transfer function modelling of the reverberating iron-K line allows us to place constraints on the black hole mass of $(3.0^{+3.7}_{-2.8} \times 10^5\ M_\odot)$ concurrently with the spin $(0.98^{+0.01}_{-0.02})$ and coronal height without inherent degeneracy. Furthermore, results for NGC 4395 fit well with the scaled black hole mass versus iron-K lag [9], and with the hypothesis that today's SMBHs are formed from rapidly spinning small mass black holes [16–18]

.

Astrophysical black holes in the mass range $\sim 10^2$–$10^6\ M_\odot$, commonly referred to as IMBHs [19], represent the link in the black hole mass between stellar-mass and SMBHs. They are of fundamental importance because they may be relics of the primordial seeds that grew into today's SMBHs [20, 21]. IMBHs are expected to reside in dwarf galaxies or dense stellar systems [22], but remain elusive due to the difficulty of direct detection. Their gravitational sphere of influence is generally too small to be spatially resolved with current instruments, precluding dynamical mass measurements. Reverberation mapping provides a powerful alternative, but in practice it is challenging for IMBHs because their variability signals are often extremely weak.

The two known prototypical IMBHs to date are in the late-type spiral galaxy NGC 4395 [23] and in the dwarf elliptical galaxy POX 52 [24]. However, by virtue of the closest proximity (4.3 Mpc), NGC 4395, hosting one of the least luminous Seyfert 1 nucleus, has the strongest observational evidence, making it the most confirmed IMBH to date. Over the past two decades, diverse methods, including optical reverberation mapping and gas dynamical modeling, consistently point to a black hole mass of $M_{\rm BH} \sim 10^4$ to a few $\times 10^5 M_\odot$ in NGC 4395 [25–29]. Observations show that the source is one of the few variable targets in this low mass regime in the sky, exhibiting exceptional X-ray variability on a typical timescale of hours to minutes [30, 31]. The

power density spectrum has a clear break at a frequency $(0.3-3)\times10^{-3}$ Hz [30, 31], which appears to be the highest characteristic frequency obtained for a typical Seyfert galaxy [31]. The power density break timescale was found to be the shortest observed among radio-quiet AGNs [32]. The time-averaged flux spectrum produced from the *ASCA* observation resolved a relativistically broadened iron line at ~ 6.4 keV with an equivalent width of 310^{+70}_{-90} eV [30]. Previous monitoring campaigns have confirmed the X-ray reprocessing scenario in NGC 4395, showing a reverberation delay between the variability of X-ray/UV/optical [33–35]. In addition, an X-ray lag was seen in the soft excess [36, 37]. NGC 4395 was observed by *XMM-Newton* [38] in four consecutive epochs (epoch 1-3: 13, 19 and 31 December 2018; epoch 4: 2 January 2019), each for an exposure of $\sim 116-117$ ks, totaling ~ 460 ks (see Extended Data Table 1). Also, simultaneous observations of ~ 25 ks of *XMM-Newton* and ~ 50 ks of *NuSTAR* [39] observations were obtained in six different flux epochs during December 10 to 30, 2022, totaling ~ 130 ks of *XMM-Newton* and ~ 300 ks of *NuSTAR* observations.

The iron-K line profile has been used as a key ingredient in inferring the geometry of the corona [40] and the innermost disc [41]. The irradiation profile of the corona generated on the inner disc is sensitive to the geometry of the illuminating source itself, imprinting information onto the shape of the iron-K emission line [42]. A strong iron-K line results from the high fluorescence yield, where the impact of intrinsic absorption is often low. This enables a clean estimate of the black hole spin a ($= Jc/GM_{\rm BH}$, where G is the gravitational constant, c the light velocity and J is the angular momentum) [43]. Reverberation and reflection modelling of the iron line give complementary measures of the black hole spin and coronal height h. While modelling such lines has been undertaken in SMBHs [2, 44–47], IMBHs are still left, as robust lag detection in them remains difficult due to relatively lower X-ray count rates. Until now, however, signs of reverberation have been found in only a few AGNs with $M_{\rm BH} < 3\times10^6\ M_\odot$ [14].

The light curves of NGC 4395 show significant variability with sufficient photons (see Extended Data Figure 1), and in epochs 2 and 3 the source went into a low flux state, making it an excellent testbed to look for relativistic reverberation. We measure a reverberation delay in the iron-K emission band using the $\sim 116-117$ ks *XMM-Newton* observations from 2018-2019. Individual observations (epochs 2 and 3), obtained during the low flux states, provide a high signal-to-noise measurement of the X-ray time lags, resulting in an iron-K lag amplitude of 23.40 ± 16.01 secs in epoch 2 and 23.4 ± 7.2 secs in epoch 3 (see Figure 2). It is furthermore apparent from the lag spectra that the iron-K lag peaks more prominently in the lowest flux observation obtained in epoch 3, whereas the other bands seem to be tending toward zero or negative lags. In contrast, high flux observations (epochs 1 and 4) do not provide high signal-to-noise detections of Fourier lags, as the detections are likely to be hampered by the low variability signal-to-noise ratio [see e.g. 48]. These two observations are, therefore, combined with the other two observations (epochs 2 and 3), which allows us to isolate the iron-K emission feature with a lag amplitude of 24.8 ± 10.0 secs (see Extended Data Figure 2).

We perform modelling of the Fourier lags using the GR transfer function code KYNREVERB [49], which computes the response of the disc to coronal X-ray flare and describes all relativistic effects around the black hole [2, 45]. The model is applied simultaneously to the lag spectra obtained from epochs 2, 3, and to the combination of four epochs (1–4). The underlying model assumes that a small X-ray source ($r << h$) at height h on the rotation axis of the black hole illuminates the disc. We set some of the parameters to the values obtained from the time-integrated reflection spectra (see Methods for detailed modelling), which include iron abundance $A_{\rm fe}$ and the 2–10 keV luminosity $L_{2-10\ \rm keV}$. During the fit, we leave spin a, height h, black hole mass $M_{\rm BH}$ and inclination i to vary freely, but are tied between the observations except h which is determined in each observation separately.

The modelling allows us to place significant constraints on the key physical parameters. We constrain the black spin at high value, $a = 0.98^{+0.01}_{-0.02}$ and the disc inclination at $i = 31.50^{+2.77}_{-3.90}{}^{\circ}$, the values are consistent with our findings from the time-integrated reflection spectra. The coronal height h has been constrained to $1.65^{+1.86}_{-0.75}$ $R_{\rm g}$ in the lowest flux observation and $22.67^{+1.83}_{-4.61}$ $R_{\rm g}$ in the combined observations posses the highest flux. We estimate the black hole mass of $M_{\rm BH} = 3.0^{+3.7}_{-2.8} \times 10^5$ $M_{\odot}$, the uncertainties of which agree with the previous measurement of $M_{\rm BH} = (2.5 - 4) \times 10^5$ $M_{\odot}$ obtained using other methods: optical reverberation technique [25], gas dynamical modelling [26], and optical/near-IR integral field spectroscopy [27]. Note that simultaneous modelling of the lag spectra helps break the degeneracy between the black hole mass and the coronal height. The best-fit modelled spectra are shown in Extended Data Figure 3, and the parameters obtained from the modelling and their posterior distributions are shown in Extended Data Figures 4, 5, and 6.

We scale the black hole mass versus iron-K lag of NGC 4395 with those obtained for SMBHs based on previous lag measurements. It has been shown that normal Seyfert 1 galaxies show a linear dependency of the iron-K emission lag amplitude τ on the black hole mass $M_{\rm BH}$ [1, 9]. Our measured mass of $M_{\rm BH} = 3.0^{+3.7}_{-2.8} \times 10^5$ $M_{\odot}$ and the Iron-K lag amplitude of 24.8 ± 10.0 secs (from the combination of the four epochs) fit well with this trend at the low mass end (Figure 3), suggesting that the linear lag dependency still holds after including IMBH in the sample (see Methods).

Understanding the nature of the X-ray corona also became practicable since the *NuSTAR* era [4, 50], the hard X-ray focusing telescope extending high sensitivity and spectral resolution far beyond 10 keV. The potential application of X-ray reflection spectroscopy has been extended having obtained high-quality spectra, constraining the coronal extent alongside the black hole spin [43]. The study of these innermost regions is realised using the `relxill` analysis package [51, 52], which is fully based on the general relativistic ray-tracing simulation in vacuum, with their internal spectral resolution allowing them to be fully applied to the *NuSTAR* instrumental responses [53, 54].

Reflection spectroscopy for NGC 4395 is employed using the six sets of observations, simultaneously covered by *NuSTAR* and *XMM-Newton* in 2022. Spectra from both instruments are jointly modelled, providing a solid constraint on the height h of the corona in each observing flux epoch. We observe that the height h increases from $6.51^{+1.11}_{-1.04}$ $R_{\rm g}$ in the lowest flux state to $26.66^{+2.71}_{-4.77}$ $R_{\rm g}$ in the highest flux state. The change in the observed height is simply the distance that varies between the disc reprocessing region and the X-ray source illuminating the disc. Additionally, fits of the broadband spectra allow us to constrain the high-energy cutoff $E_{\rm cut}$, which occurs at a minimum value of $54.65^{+9.13}_{-5.63}$ keV, manifesting itself as a low temperature corona. In the conventional scenario, when the temperature is low ($kT_{\rm e} < 100$ keV), the X-ray source is compact in a radiative sense [50], which would imply that there are intense interactions between photons and photons as well as particles – leading to electron-positron pair production [e.g. 55]. The determining ingredient of the nature of such a corona is the dimensionless compactness parameter $l = L\,\sigma_T / R\,m_e\,c^3$ [56]; where L is the luminosity, R the radius of the illuminating X-ray source, σ_T is the Thomson cross-section, and m_e is the electron mass. Comparing L with the Eddington limit $L_{\rm Edd}$ and exchanging R with $R_{\rm g}$ (Eq.2 in Ref.[50]), l for NGC 4395 appears to be ~ 1, considering $L = 1.2 \times 10^{40}$ erg s^{-1} [57]. If we place NGC 4395 in the compactness-temperature diagram ($l - \Theta$; where $\Theta = kT_e/mc^2$ [50]) it fits well therein, consistent with the pair production process which acts as a l-dependent thermostat [58, 59].

The dynamics of the black hole corona is now being revealed in some detail [60]. Flux-resolved spectroscopy showed a decrease in the coronal height as the source flux decreased on a short timescale (∼hours) [4], which appeared with a variation only between ~ 2.3 $R_{\rm g}$ and ~ 5.1 $R_{\rm g}$. Geometrical changes in the X-ray corona were also observed over the course of long-term flux changes, attained by averaging observations over decades [5]. However, timing-based results provided a better dynamic picture in response to inner accretion flow around an SMBH, showing a rapidly changing coronal height [61]. The reverberation modelling carried out for the IMBH source NGC 4395 appears significant, revealing changes in the coronal height by a factor of ~ 14 on a timescale of a few days. Reflection spectroscopy of the 2022 observations, which were taken in an interval of 3/4 days, shows that coronal height varies considerably (roughly by a factor of ~ 4). The maximum height to which the corona moves is $26.66^{+2.71}_{-4.77}$ $R_{\rm g}$ which combined with the timing results shows a far more significant variation where the minimum height to which the corona moves down is $1.65^{+1.86}_{-0.75}$ $R_{\rm g}$. Combined spectral-timing results further suggest that the X-ray corona moves much closer to the black hole, when the source is in low flux state, and successively moves further away when the bright state is regained (see Figure 1).

Black hole spin measurements are important diagnostics of the growth and formation of black holes [62]. It has been realized from the X-ray reflection method that SMBHs refer to two families; one with a mass range below 30 million solar masses, which appears to stay close to maximal rotation ($a \gtrsim 0.9$), and the other is more massive black holes having a moderate range of spin ($a \sim 0.4 - 0.7$) [43]. The hypothesis being that high-mass and low-spin SMBHs of the present age were formed from merger

of smaller black holes or through the process of more isotropic chaotic accretion [16–18, 62]. The rapidly spinning low mass black hole ($a \sim 0.98$) in NGC 4395 is interesting and supports this notion. We plot the black hole spin against the mass of SMBHs based on previous measurements (produced from Ref.[63]) and include results for NGC 4395, which fits in the extreme low mass end where the spin is high (shown in Figure 4). Detailed discussion of it, however, is beyond the scope of this work.

In summary, we have employed two powerful approaches simultaneously: X-ray reverberation modelling and reflection spectroscopy; both can concurrently provide crucial insights into the innermost region, black hole properties, and the geometrical arrangement of the disk-corona system. While these two techniques have been used to understand the physical processes around SMBHs in normal Seyfert 1 galaxies [5, 61, 64] and stellar mass black holes in XRBs [65, 66], applying both techniques simultaneously to a black hole mass of the IMBH regime gives complete details of the inner accretion flow and disc-corona system, which we present here for the first time in the closest prototype IMBH in NGC 4395. While this dynamic corona has been seen before in SMBHs and stellar-mass black holes, our study is the first to reveal the same phenomena in an IMBH. Reverberation modelling alone places a strong constraint on the height of the corona in this source. This is well reconciled with the reflection spectroscopy; combining results from broadband spectral analysis with response modelling we observe that the source is rapidly evolving, where the height of the illuminating X-ray source changes remarkably owing to dynamics of the accretion flow. Modelling of the iron-K reverberating line puts strong constraints on the key parameters; the black hole spin, mass, and coronal height, where no inherent degeneracy appears between them, enabled by simultaneous modelling. We find that NGC 4395 fits well in the scaled iron-K lag versus black hole mass relation, also supporting the concept that rapidly spinning black holes of small mass grew to form SMBHs.

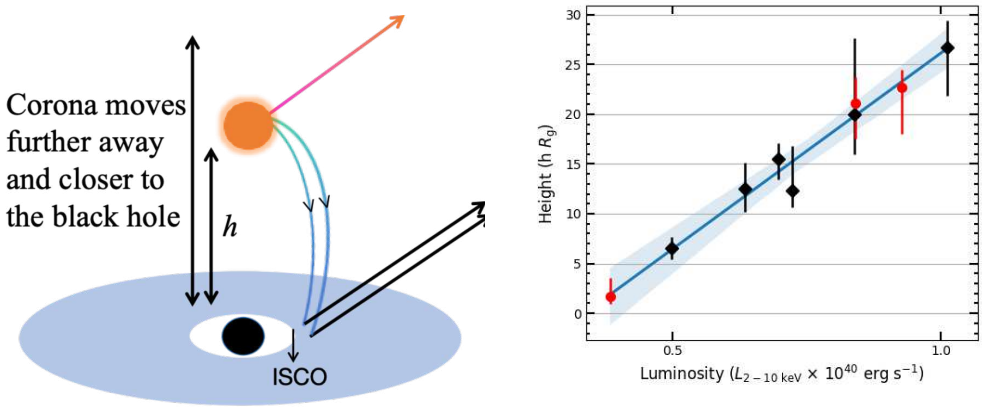


Figure 1. *Left:* Schematic geometrical arrangement of the X-ray reverberation model. A compact X-ray source (a.k.a. X-ray corona) at height h isotropically emits X-rays, which are concentrated by the strong gravity onto the geometrically thin and optically thick accretion disc where they are back-scattered. The gravitational light bending effect causes much of the emission to strike the disc near the ISCO when the X-ray source is close to the black hole. The intrinsic X-ray continuum from the corona and the reprocessed emission from the disc reach the rest frame observer with a certain path length difference between them; the light crossing time to cover this distance is the X-ray reverberation delay. The X-ray source moves closer to and further away from the black hole as a consequence of the general relativistic effect. *Right:* 2–10 keV X-ray luminosity versus height of the X-ray corona obtained from combined spectral and timing methods. The plot shows that the source appears brighter as the height increases due to the light bending effect reducing. Height measured from the relativistic transfer function modelling of the lag spectra (red circles) is combined with the measurement from the reflection spectroscopy of the time-averaged flux spectra (black diamonds). The data points and 1σ error bars are fitted with a linear regression line (blue line), and the 99% confidence interval is plotted, shown by the shaded region.

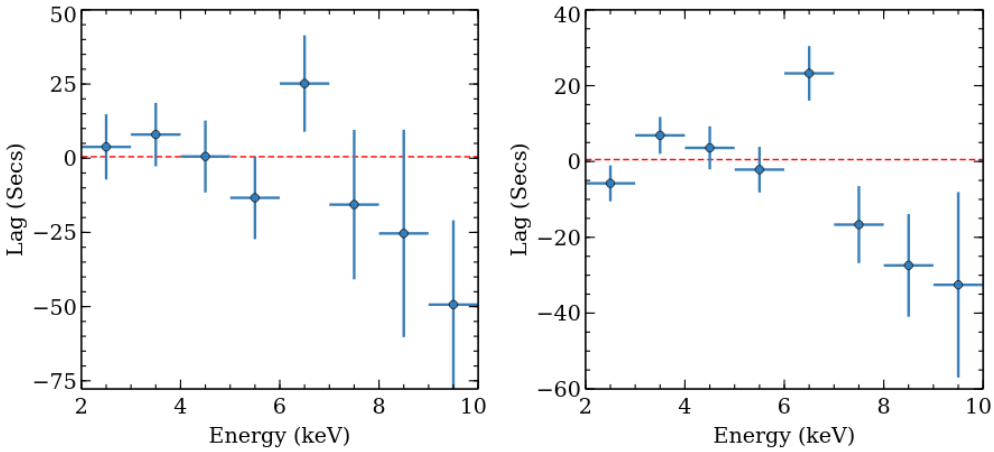


Figure 2. Fourier time lags versus X-ray energies for NGC 4395. Observed lags are computed between the narrow energy bands (each of width 1 keV, from 2 to 10 keV energy range) and the 2–10 keV reference band, excluding the bands of interest. The lags are calculated from the cross-spectrum, averaging over frequency bins from 0.3 to 6.5×10^{-4} Hz for observation 0824610201 (epoch 2, *left*) and from 1.5 to 22×10^{-4} Hz for observation 0824610301 (epoch 3, *right*). Positive lags indicate that the bands of interest lag behind the reference band by the corresponding value on the Y-axis. The spectra show that the lag peaks at the 6–7 keV energy band (reflection-dominated band inclusive of the iron-K emission line), which responds later than the intrinsic continuum from the corona (powerlaw-dominated bands) with an average time delay of $\sim$ 23.4 secs (for both the observations shown), suggesting reverberation from the inner accretion disc.

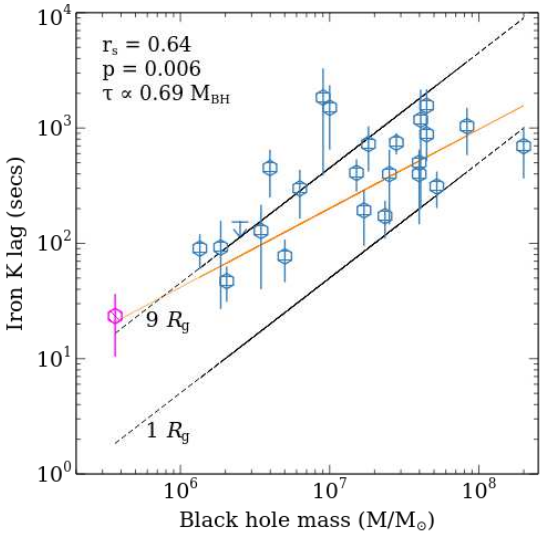


Figure 3. Iron-K lag amplitude as a function of black hole mass. Lags for normal Seyfert 1 galaxies harboring SMBHs are obtained from the previous reverberation mapping results (shown in blue). Most of the lags are reproduced from Ref.[9] with the addition of iron-K lag in IZw 1 [64]. Lag measured for NGC 4395 from the combination of four *XMM-Newton* observations (0824610[101-401]) is overplotted (shown in Magenta) against the black hole mass of $3.0 \times 10^5\ M_\odot$ obtained from the reverberation modelling. The plot shows that lag increases with the black hole mass, suggesting a linear dependency of the iron-K lag on the black hole mass, wherein the lag observed in NGC 4395 well fits at the low mass end. Black diagonal lines represent the lags at 1 R_g and 9 R_g. A linear model is used on the log-log plot, indicated by the orange line, which gives a lag-mass relation, $\tau \propto 0.69\ M_{BH}$. The Spearman correlation test provides a rank correlation coefficient $r_s = 0.64$ with probability $p = 0.006$.

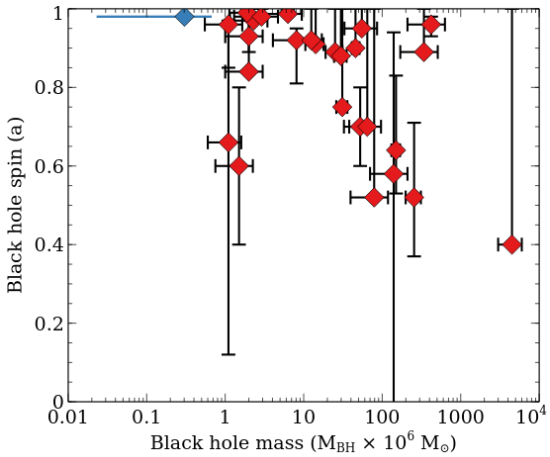


Figure 4. Mass of supermassive black holes versus spin from the published results, over which results obtained for NGC 4395 ($M_{\rm BH} = 3.0^{+3.7}_{-2.8} \times 10^5 M_\odot$, $a = 0.98^{+0.01}_{-0.02}$) are plotted (shown in blue). The plot is reproduced from [63] and updated with the results of other AGNs from [64, 67–69]. Following the conventions in the primary literature, error bars on all masses are quoted at 1σ confidence, and error bars on spins are quoted at 90% confidence.

Methods

Observation and data reduction

XMM-Newton

NGC 4395 has been observed multiple times by *XMM-Newton* in several different flux states. Longer observations were obtained in 2018-2019 in four different epochs (0824610101, 0824610201, 0824610301, 0824610401) for exposures of 116-117 ks, a total dration of $\sim$ 460 ks was obtained. Six other observations were obtained in 2022 at different flux states, each with 25 ks, and for a total duration of 130 ks. The *XMM-Newton* datasets are presented in Extended Data Table 1. The short exposures from 2022 have low signal-to-noise and are not useful for X-ray reverberation lag analysis, and therefore their use is limited to spectral analysis. However, the long observations of 2018-2019 can be of particular use in the search for reverberation lags. Epoch 1 of these observations captured a flare during which the source flux level increased 3.5 times the average. The flux declined in epoch 2, with its light curve providing a mean count rate of 0.37 c/s. During epoch 3, the source was observed to enter into the lowest flux state, where the mean count rate was estimated to be 0.2 c/s. After this, the flux level increased again as the source entered the flaring state again in epoch 4. The mean count rate in this state is estimated to be 0.67 c/s.

The *XMM-Newton* data reduction process was completed using the Science Analysis System (SAS v.20.0.0). The large effective area and unprecedented sensitivity of the EPIC camera on board *XMM-Newton* are of particular use to implement X-ray timing analysis. We used EPPROC task to generate event files, which were screened and cleaned for the high particle flaring background by applying the standard filtering criteria "(PATTERN <= 4)&&(FLAG == 0)" for EPIC PN. The cleaned events are generally used to extract the source and background counts. We obtained source counts from a circular extraction region of 40 arc seconds, while another source-free region of 50 arc seconds was used to obtain background counts. This selection criterion was imposed to maximize the signal-to-noise ratio (S/N). Following the EVSELECT task for extraction, the background-subtracted light curves were obtained using the SAS task EPICLCCORR. We performed two other SAS tasks RMFGEN and ARFGEN to produce instrumental responses, including RMF (response matrix files) and ARF (auxiliary response files) which are required to oversample instrumental resolution. Finally, the source and background spectra were grouped using the command SPECGROUP under the condition that each spectral bin contains at least 20 counts.

NuSTAR

XMM-Newton observations from 2022 of NGC 4395 were coordinated with *NuSTAR*, each for a 50 ks exposure, for a duration of 300 ks in total. The details of the datasets are provided in Extended Data Table 1. Six observations were obtained by *NuSTAR* (Observation IDs: 60802027002, 60802027004, 60802027006, 60802027008, 60802027010, 60802027012) at different flux epochs, which are of particular importance

for obtaining different flux spectra to be used for flux-resolved spectral analysis. The standard *NuSTAR* pipeline NUPIPELINE script was run in the initial data reduction stage, providing Level-1 data products. The data were screened for high-background flaring events and calibrated by applying the standard filtering criteria. The pipeline processing was succeeded by the use of *NuSTAR* data analysis software NUSTARDAS (v.1.10) with the calibration database (CALDB; version 20250415). From the clean event files obtained for the two *NuSTAR* focal plane arrays FPMA and FPMB, we extracted counts from a circular region of 49 arc seconds centered on the source, while the background counts were extracted from a larger source-free region of 65 arc seconds. We used the NUPRODUCTS task to produce the final data products, including the source spectra and the background spectra. The spectra were then grouped using the GRPPHA tool so that at least 50 counts per spectral bin are contained.

Fourier lag spectra

To apply the Fourier implementation of the timing analysis, we follow the procedure detailed in Nowak et al. [70] and further presented in Uttley et al. [1]. We generate light curves in narrow energy bands with a time binsize of 10 s, each of width 1 keV, across the 2–10 keV range. Lags are computed between the narrow bands and a reference band. The reference band is taken across the 2–10 keV, while subtracting the current narrow energy band of interest. The choice of a broad reference band is to maximize the signal-to-noise ratio and to avoid correlated noise between the narrow energy bands. We take the Fourier transform of each light curve and multiply one by the complex conjugate of the other. This product constructs a cross spectrum, encoding the phase information, typically the phase difference between the two light curve bands. The cross-spectrum is then averaged over some pre-defined frequency bins in logarithmic space. Generally, phase lag $\phi(f)$ is converted into time lag $\tau(f) = \phi(f)/2\pi f$, where f is the center of defined frequency bins in the logarithmic space.

X-ray Reverberation lag

The high signal-to-noise ratio observations obtained for a longer duration ($\sim$ 460 ks) in 2018-2019 offer us the opportunity to undertake the X-ray reverberation approach. The variability of the light curves of NGC 4395 is evident in each epoch of the observations (shown in Extended Data Figure 1), with the flux decaying from the first to the third observation and then increasing again in the fourth observation. We perform the Fourier analysis by first computing the lag-energy spectrum. The sign convention adopted here is that positive lag means that the band of interest lags the reference band. Figure 2 shows the lags versus energies computed from epochs 2 and 3 of the observations obtained in the low flux state. The whole lag spectra are observed to shift down to zero lags, while leaving only the iron-K emission peaking band 6–7 keV. The iron-K lag amplitude is measured to be 23.40 ± 16.01 secs in epoch 2 with the highest signal-to-noise ratio, which is obtained by averaging the cross-spectrum over the Fourier frequency range from 0.3 to 6.5×10^{-4} Hz. Similarly, the lag spectrum computed from the lowest flux observation in epoch 3 shows the iron-K emission feature, which appears more prominently with a lag amplitude of 23.4 ± 7.2 secs,

provided by the cross-spectrum over frequency range 1.5 to 22×10^{-4} Hz. Low flux observation has been found to be particularly relevant in producing the reverberating line, which was observed in the Seyfert galaxy NGC 4151 with a first detection of Fe K lag [7]. The frequencies used in calculating the lag spectra correspond to a short timescale variability (∼hours or less). A broad range of frequencies are taken, over which the cross-spectrum is averaged to optimize the signal-to-noise. The quoted frequency ranges also match closely with the break frequencies in the power density spectrum, 3×10^{-4} Hz [30] and $(0.5 - 3) \times 10^{-3}$ Hz [31], representing the characteristic timescales proportional to the innermost disc-size that is scaled with the black hole mass $\sim 10^4 - 10^5\ M_{\odot}$. It was also found that the frequencies at which X-ray lags emerge are different during different flux states [71], where higher flux intervals produce lags at lower frequencies compared to low flux intervals. The case for NGC 4395 is although different, where both epochs 2 and 3 were obtained in a low flux state, the observed flux in epoch 2 is still higher than in epoch 3, resulting in lags at relatively lower frequencies. The first and fourth epochs of the observations (0824610101, 0824610401) obtained during high flux periods do not provide a high signal-to-noise measurement of the time lags. However, both observations can be combined with the low flux observations (0824610201, 0824610301) to maximize the signal-to-noise and place a better constraint on the lag spectra. The lag-energy spectrum produced from the combined observations is presented in the left panel of Extended data Figure 2, which shows the iron-K line feature with a clear delayed response. The lag spectrum picks out the 6–7 keV delay of 24.8 ± 10.0 secs, calculated from the cross-spectrum averaging over frequency range 0.3 to 6.5×10^{-4} Hz. It should also be noted that the observed lag amplitudes are small and are most unlikely to arise from a distant reflector, which is responsible for producing the narrow line at $\sim$ 6.4 keV seen in the photon spectrum [32]. Relativistic reverberation of the Fe K line has been observed in the source in which the spectral feature is not relativistically broadened (e,g, NGC 4151 [7]). Alternately, if the lag is associated with the narrow line, then significant line flux changes would have been seen in the X-ray spectra. However, over the six simultaneous epochs with the *XMM-Newton*/*NuSTAR* campaigns, the line flux here is noticeably constant. Further, shorter lags can be associated with a distant reflector (a few $\sim$ 100 to 1000 $R_{\rm g}$) if the reflecting medium is erratic [72]. But difficulties arise in such cases because the lag has an oscillatory behaviour which will prompt the lag measurement over a wide frequency range, resulting in the average lag value becoming zero. The arguments on the presence of high frequency lags within this framework can be found in Ref.[73].

Despite long exposure, in addition to a high count rate and extreme variability, which qualifies the observation for a lag detection to be statistically significant, the appearance of the reverberation lag is not seen in all circumstances. Although another high signal-to-noise ratio observation of NGC 4395 was obtained in 2003 for $\sim$ 113 ks, no iron-K lag detection has been made in previous work [9]. This observation is therefore no longer used to compute the lag spectra here. Different variability processes could be involved with being responsible for the non-detection of the reverberation lags. In general, lag detection is feasible when the directly observed continuum has intrinsic

variability, which also needs to be correlated with the disc-reflected emissions. But it is unlikely that a weak variability signal, the intrinsic continuum, will result in any lag detection. The variability is also attributed to the geometrical change in the height or spatial extent of the X-ray emitting source, which does not give rise to any correlated variability in disc emissions, precluding lag detection. This has been interpreted to be the underlying variability mechanism involved in NLS1 MCG-6-30-15 as a result the most expected iron-K lag did not appear [see 74], and could also explain the non-detection with the 2003 observation of NGC 4395. It has also been noticed that the prominent iron-K reverberation lag detected in earlier observations disappears again in later epochs (e.g. NGC 4151 [75] and NGC 5506 [76]). The variability caused by geometrical height changes of the corona imprints on the powerlaw emission when gravitational light bending [77] is at play – causing most X-ray emissions to focus on the innermost disc. This generally occurs in a low flux state when the X-ray source is closest to the black hole, making the reverberation lag more apparent – as seen in the iron-K lag detection in NGC 4151 [7] and in epochs 2 and 3 of NGC 4395 in this work. In the high flux state the corona will be at a higher height where most power-law emissions will be directed toward the observer, undermining correlated variability in the disc-reflected emissions, which perhaps prevents direct lag measurement in the individual epochs 1 and 4 of NGC 4395 despite good signal-to-noise ratio. However, more observations in the future for longer exposures will provide further insight into this scenario.

GR impulse response modelling

We turn now to the impulse response modelling of the observed lag-energy spectra. This is important to account for the lag dilution effect, where the impulse response takes into account the full treatment of the general relativistic (GR) effect around a spinning black hole [2]. The GR ray-tracing simulation of the reverberation lags was performed in Ref.[78] considering the emission of the directly observed powerlaw continuum from the corona and the disc-reflected emission, towards inferring the scenario in which the X-ray corona extend radially as well as vertically. The light curve band of interest and the reference bands taken in our analysis are generally referred to as the intrinsic continuum associated with the X-ray source and the disc-reflected fluorescence line emission. Both components have a fraction contributed by the other, which diminishes the observed lag amplitude. X-ray observations with the current detectors as yet do not allow one to simultaneously trigger at different rapid cadence, unable to provide high-cadence light curve for the powerlaw and the reflected bands. While this is the case for optical reverberation mapping, light curves from low and high-cadence observations can be used to separate out the reprocessing timescale. The potential of GR transfer function modelling has emerged as a useful means to simultaneously describe the lags contributed by both components [see 1].

We fit the lag-energy spectra in XSPEC (v.12.14.1) [79] using the transfer function model KYNREVERB. The model encrypts the full treatment of the general relativistic ray tracing calculations in vacuum and can account for the lag dilution effect.

Reflections occurring at each radius of the ionized disc are self-consistently calculated using the reflection table `xillver` [52, 80]. We carry out simultaneous fitting of the lag spectra comprising the iron-K reverberating line obtained from *XMM-Newton* epoch 2, epoch 3, and the four combined epochs (1–4) of the 2018-2019 observations. Some of the parameters are fixed to the values obtained from the time-averaged flux spectra, including the iron abundance A_{fe} and the 2–10 keV luminosity $L_{2-10\ \mathrm{keV}}$ for each observation similar to [61]. Additionally, we fix the outer radius R_{out} of the disc at $400R_{\mathrm{g}}$. The inner radius takes its value down to a limit of $\sim 1R_{\mathrm{g}}$ when initially free, then left frozen at the corresponding value. We allow the height of the corona h, the black hole mass M_{BH}, spin a, and disc inclination i to vary freely. These parameters are tied between the observations, except for height h, which is allowed to vary independently between observations. During the fit, we used a multiplying constant, which is fixed at 1 for one spectrum and left free for the other two spectra. The height of the corona, h, and the luminosity observed in the 2–10 keV band, $L_{2-10\ \mathrm{keV}}$, are listed in Extended Data Table 2. We plot h versus $L_{2-10\ \mathrm{keV}}$ for the data obtained from response modelling and the reflection spectra together, shown in Figure 1. We perform a linear regression fit to the data using a model of the form $h = a \times L_{2-10\ \mathrm{keV}} + b$, where a is the slope and b the intercept. The fit for h and $L_{2-10\ \mathrm{keV}}$ provides us with a slope of $a = 4.11 \pm 0.39$ and an intercept $b = -13 \pm 2.8$.

The best-fit modeling yields good statistics, yielding a reduced χ^2_ν/d.o.f. $= 35/36$. The errors estimated for the free parameters are obtained at 68% confidence interval. For error estimation, we perform the MCMC analysis using the XSPEC_EMCEE code in XSPEC. XSPEC_EMCEE script is a pure Python implementation of Goodman & Weare's Affine Invariant Markov Chain Monte Carlo (MCMC) Ensemble sampler. We take 50 walkers and run the MCMC chain for 10,000 iterations, followed by burning the first 1000. We generate the corner plots for the key physical parameters and derive their posterior distributions from the MCMC analysis at the 1σ, 2σ, and 3σ levels (shown in Extended Data Figures 4, 5 and 6). As seen in the plots, there appears no strong degeneracy between the parameters a, M_{BH}, h and the inclination i. Further examining the degeneracy between the black hole mass M_{BH} and coronal height h, they are found to be well constrained, and simultaneous modelling breaks the inherent degeneracy between them.

X-ray spectral modelling

The timing analysis discussed in previous sections has demonstrated how X-ray lags evolve with energy and frequencies. We perform modelling on broadband X-ray spectra over the energy range 2–50 KeV covered by *XMM-Newton* and *NuSTAR*. The *XMM-Newton* observations obtained in 2022 provide limited photon counts. However, combining these with contemporaneous *NuSTAR* observations from the two detectors, FPMA/FPMB optimizes both photon counts and spectral resolution. The model is applied first to the 2–10 keV *XMM-Newton* spectra, followed by simultaneously to the 3–50 keV *NuSTAR* spectra. We use a constant to compensate for normalization of the spectra provided by three different instruments due to their cross-calibration

uncertainties.

We perform a spectral analysis using reflection modelling. Reflection spectroscopy is another powerful tool that can be applied to understand the geometry of the black hole corona and to probe the accretion disc within a few gravitational radii of the black hole where most X-ray emission releases. The atomic features encoded in the X-ray spectrum can be fully characterized to have information on the accretion state and the driving mechanism, where different flux X-ray spectra can provide insight into the evolution of the X-ray source. Reflection spectroscopy is the key for spin measurement using the broad iron line profile within the scenario in which X-ray emissions arise from the close vicinity of the black hole. The emissions from around ISCO imprints in the reflection spectrum, with a more prominent feature being that the iron-K line profile peaks at centroid energy ~ 6.4 keV, dictated by the ionization state. The line becomes relativistically broad as we get closer to the black hole. It is also said that the location and structure of the X-ray source are the key settings of reflection spectroscopy [43].

NGC 4395 shows the iron-K line emission feature in its spectrum, shown in Extended Data Figure 2 (right panel), which is the rebinned version of the ratio of the *XMM-Newton* X-ray spectrum to a simple powerlaw model. The *NuSTAR* spectrum also presents reflection features, including a Compton hump above 10 keV as shown in Extended Data Figure 7 (right panel). The presence of reflection features suggests that X-rays emerge from the inner part of the disc as a result of irradiation from a compact X-ray source at a height h from the central black hole (see Figure. 1, left panel). The broadband spectrum, therefore, requires fitting for the X-ray continuum emission by the powerlaw with a high-energy cutoff parameter, $E_{\rm cut}$ that determines the coronal temperature and simultaneously the reflection spectrum. We use `relxilllp` variant of the relativistic reflection code `relxill` [51, 52] to model the observed spectra which self-consistently constrain the location of the X-ray source (height h of the corona). The state of the art of this model posits that the X-ray spectrum is resulting from the reflection from the disc being due to continuous irradiation by the X-ray source described by `xillver` [80, 81], which is convolved with the relativistic ray-tracing code `relline` [81] to take into account the extreme relativistic effects around the black hole, including the gravitational redshift and Doppler shift. In addition, we use a partially covering absorber component (`zxipcf` [82]), while the galactic absorption column is fixed at 1.85×10^{20} cm^{-2} [25] using `Tbabs` [83].

The X-ray spectrum of NGC 4395 below $\sim$ 2 keV appears to be highly complex, with the contributions of multiple absorption components that are warm absorptions, neutral absorption, and an emission feature at $\sim$ 0.6 keV [32, 84]. Typically, these components have a substantial impact on the X-ray spectrum, leading to an inadequate determination of the spectral behavior. In general, the underlying features are not seen to appear beyond $\sim$ 2 keV. In particular, the iron-K emission line, which peaks at 6–7 keV, is observed to be a clean part of the spectrum. Furthermore, reprocessed X-ray emission in an ionized disc that dominates at $<$ 1 keV depending

on the density and structure of the disc [65, 85]. While this cannot be accounted for by using the `relxilllp` model, spectral fitting over the 2–50 keV band can place a robust constraint on the reflection X-ray spectra, including the iron-K feature and reflection hump.

Reflection spectroscopy with `relxilllp` provides a good description of the spectra over the 2–50 keV bandpass. Representative spectra of joint modelling from two different flux states are displayed in Extended Data Figure 7 (left panel). The joint spectral fitting of the *XMM-Newton* and *NuSTAR* spectra enables us to constrain the height h of the X-ray source. We observe that the coronal height increases as the source becomes more X-ray luminous, with $h = 6.51^{+1.11}_{-1.04}$ $R_{\rm g}$ in the lowest luminosity state to $h = 26.66^{+2.71}_{-4.77}$ $R_{\rm g}$ in the highest luminosity state (indicated by black error bars in Figure 1; right panel). The black hole is found to be rapidly spinning ($a \geq 0.98$) at an inclination angle $i \geq 30^{\circ}$. Broadband X-ray spectra also allow us to constrain the high-energy cutoff parameter $E_{\rm cut}$ to be low, the minimum value of which has been obtained at $54.65^{+9.13}_{-5.63}$ keV, suggesting that the X-ray source is radiatively compact [50]. During spectral fit, some parameters are tied between *XMM-Newton* and *NuSTAR* observations, including iron abundance A_{fe} (=3.01), inclination i and spin a; these should also not vary over the course of the observations. We fix the outer radius $R_{\rm out}$ to 400 $R_{\rm g}$ and the inner radius $R_{\rm in}$ to the value of ISCO (innermost stable circular orbit). We note further that inclusion of a narrow feature does not improve our spectral fit; rather relativistic reflection modelling is adequate to provide a satisfactory fit to the joint *XMM-Newton* and *NuSTAR* spectra across 2–50 keV.

The key parameters obtained from the best-fit spectra are quoted in Extended Data Table 3. We perform the spectral fit in XSPEC employing the regular χ^2 method. We estimate the errors in the parameter space by performing the MCMC analysis using the XSPEC_EMCEE code. Here we again use 50 walkers and run 10,000 iterations, then burn the first 1000. The errors quoted are estimated at a 68% confidence interval.

Iron-K lag versus black hole mass

Previous lag measurements showed a linear dependency of the iron-K band lag on black hole mass for normal type 1 Seyfert galaxies [1, 9]. This has been interpreted in a scenario where high-frequency iron-K lag originates as a result of relativistic reverberation in the close vicinity of the black hole. In this work, the lag versus black hole mass relation is reproduced from the published results (listed in Ref.[9]), with an additional result for NLS1 IZw 1 [64]. In the same plot, the observed 6–7 keV lag amplitude of 24.8 ± 10.0 secs for NGC 4395 (obtained from four combined epochs) is overplotted against the measured black hole mass of 3.0×10^5 $M_{\odot}$ obtained from reverberation modelling. The resulting plot is produced in Figure 3, showing that the linear mass dependency of the lag remains, where the iron-K lag increases with the black hole mass. It is seen that by extrapolating the lag versus mass relation for normal Seyfert 1s, the black hole mass of NGC 4395 can be obtained well below the low mass end of the SMBHs. We use a linear model of the form $y = a + b \times x$ to fit

the lags in the logarithmic space (indicated by the orange line). This derives a scaling relation of lag τ and black hole mass $M_{\rm BH}$ as $\tau \propto 0.69\, M_{\rm BH}$ — consistent with Ref.[9], who similarly scaled the lags as a function of the SMBH mass, $\tau \propto 0.7\, M_{\rm BH}$. We also perform Spearman's rank correlation test between lags and black hole mass, which provides a rank correlation coefficient r_s of 0.64 at a probability p = 0.006, which agrees well with the SMBHs [9]. The lags at $1r_g$ and $9r_g$ are calculated for all black hole sources, which are shown by the black diagonal lines. Overall, the linear trend remains after including IMBH in the sample.

Acknowledgments

We acknowledges the support from the National Key R&D Program of China No. 2023YFA1607903, 2022YFF0503402. SB acknowledges support from the China Postdoctoral Science Foundation General Fund (grant no. 404985), Shanghai Postdoctoral Excellence Program (grant no. 2024686), Shanghai Postdoctoral Introduction Project, China National Postdoctoral Introduction Project and National Foreign Expert Project, Ministry of Science and Technology (grant no. 20240238). SB thanks Prof. Ranjeev Misra for the initial discussion on frequency-resolved Fourier lag analysis. HXG acknowledges the National Natural Science Foundation of China (NFSC, No. 12473018 & No. 12522304) and Overseas Center Platform Projects, CAS, No. 178GJHZ2023184MI. MFG is supported by the National Science Foundation of China (grant No. 12473019), the Shanghai Pilot Program for Basic Research-Chinese Academy of Science, Shanghai Branch (JCYJ-SHFY-2021-013), the National SKA Program of China (Grant No. 2022SKA0120102), and the China Manned Space Project with No. CMS-CSST-2025-A07. This research has made use of data and software provided by the High Energy Astrophysics Science Archive Research Center (HEASARC), which is an online multi-mission archive facility of the Astrophysics Science Division at NASA/GSFC. The work has been derived from observations obtained from NASA *XMM-Newton* and *NuSTAR*.

Author contributions

SB and HG originated the idea of this work. SB programmed the project, led the data analysis and performed reverberation modelling, and drafted the manuscript. ACF contributed significantly to the interpretation and discussion of the results of the reverberation and reflection spectroscopy and provided substantial input to the texts. HG provided contribution to the manuscript, including structural organization, logical coherence, refinement of figures and tables, and revisions to parts of the text. YZ commented on the timing analysis and contributed to the discussion. EMC commented on the Fourier lag measurements and broadly reviewed the manuscript. FV, MG, UK and GM commented on the spectral timing results and assisted in manuscript preparation. All authors reviewed the manuscript and participated in the discussion at all stages.

Competing Interests

The authors declare that they have no competing financial interests.

Correspondence

Correspondence and request for materials should be addressed to SB (samuzal.braua@gmail.com) or HXG (hengxiaoguo@gmail.com)

Data availability statement

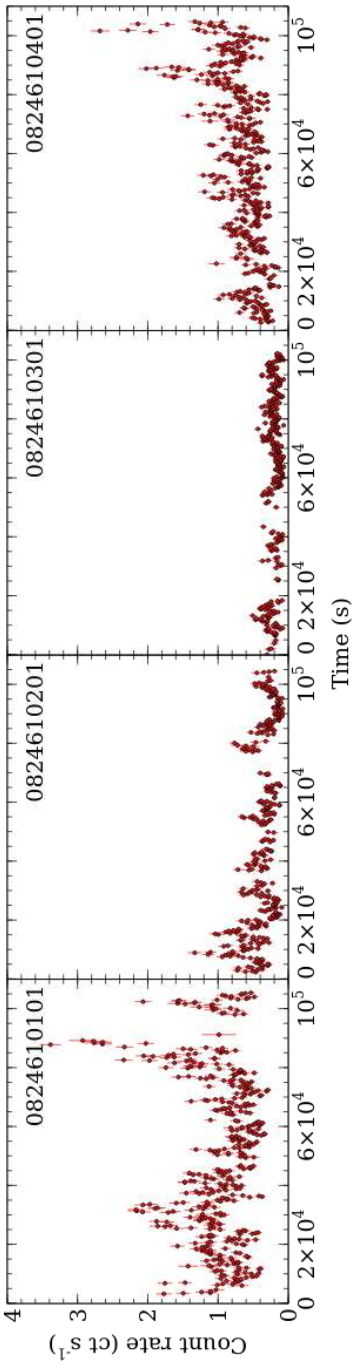
The data presented in Extended Data Table 1 were obtained from *XMM-Newton* and *NuSTAR* observations. *XMM-Newton* observations can be retrieved from the *XMM-Newton* science archive (http://nxsa.esac.esa.int/nxsa-web/). *NuSTAR* observations can be retrieved from HEARASC (https://heasarc.gsfc.nasa.gov). All data from *XMM-Newton* and *NuSTAR* used in this study are publicly available. The other data used in the figures in this manuscript can be obtained on request from the corresponding author.

Code availability

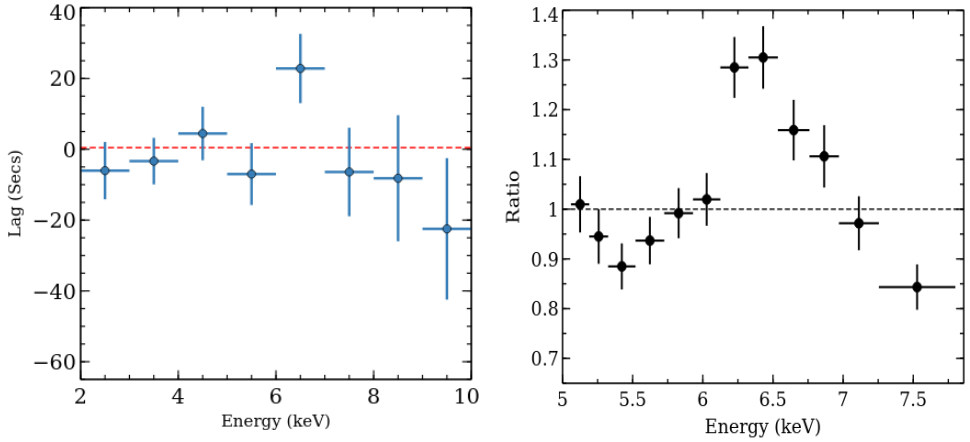
All the packages used for the standard data reduction for respective telescopes are available from their websites. Spectral fitting was performed in XSPEC which is freely available at (https://heasarc.gsfc.nasa.gov/docs/software/heasoft) as apart of HEASOFT software. The relativistic reflection model RELXILLLP is part of the RELXILL package (http://www.sternwarte.unierlangen.de/~dauser/research/relxill/). Fourier lags were computed using PYLAG available at https://github.com/wilkinsdr/pyLag. The general relativistic transfer function modelling was conducted using KYNREVERB code publicly available at https://projects.asu.cas.cz/stronggravity/kynreverb. MCMC analysis for error estimation was performed using python based EMCEE code (http://emcee.readthedocs.io/en/stable/index.html), the XSPEC execution of which can be found at https://github.com/jeremysanders/xspec_emcee.

Extended Data Table 1. Observations from *XMM-Newton* and *NuSTAR* used for timing and spectral analysis. The count rates are obtained from the 2–10 keV spectra from *XMM-Newton* and 3–50 keV spectra from *NuSTAR*.

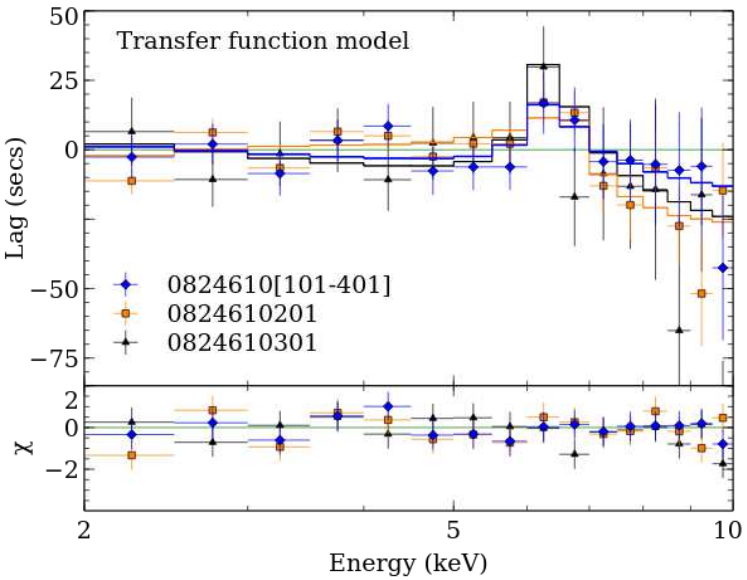
	Observation ID	Date of observation	Duration	Count rate
		(yyyy-mm-dd)	(ks)	(c/s)
XMM-Newton	0824610101	2018-12-13	117.00	0.342
	0824610201	2018-12-19	116.80	0.243
	0824610301	2018-12-31	117.19	0.128
	0824610401	2019-01-02	116.00	0.439
	0913601001	2022-12-10	11.10	0.169
	0913600101	2022-12-10	33.00	0.169
	0913600501	2022-12-14	30.00	0.013
	0913600601	2022-12-19	38.80	0.073
	0913600701	2022-12-22	28.00	0.115
	0913600801	2022-12-26	28.00	0.081
	0913600901	2022-12-30	28.00	0.107
NuSTAR	60802027002	2022-12-10	48.64	0.076
	60802027004	2022-12-14	46.06	0.138
	60802027006	2022-12-18	50.97	0.070
	60802027008	2022-12-22	52.00	0.090
	60802027010	2022-12-26	45.64	0.053
	60802027012	2022-12-30	55.39	0.071



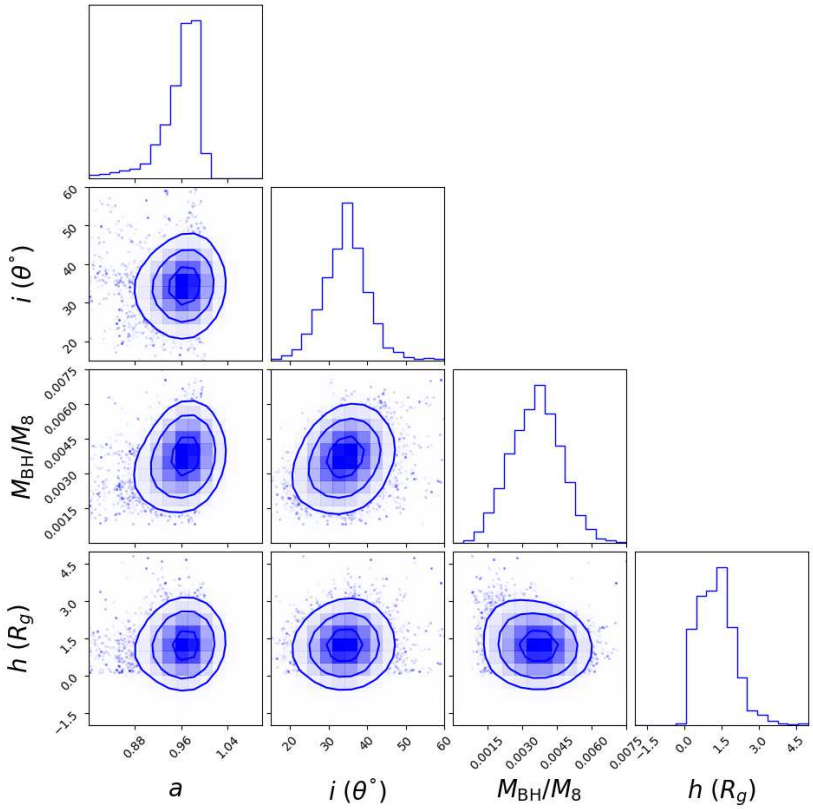
Extended Data Figure 1. *XMM-Newton* light curves of NGC 4395 produced from four epochs of the 2018-2019 observations. The light curves are produced using a time bin size of 200 secs for visual representation.



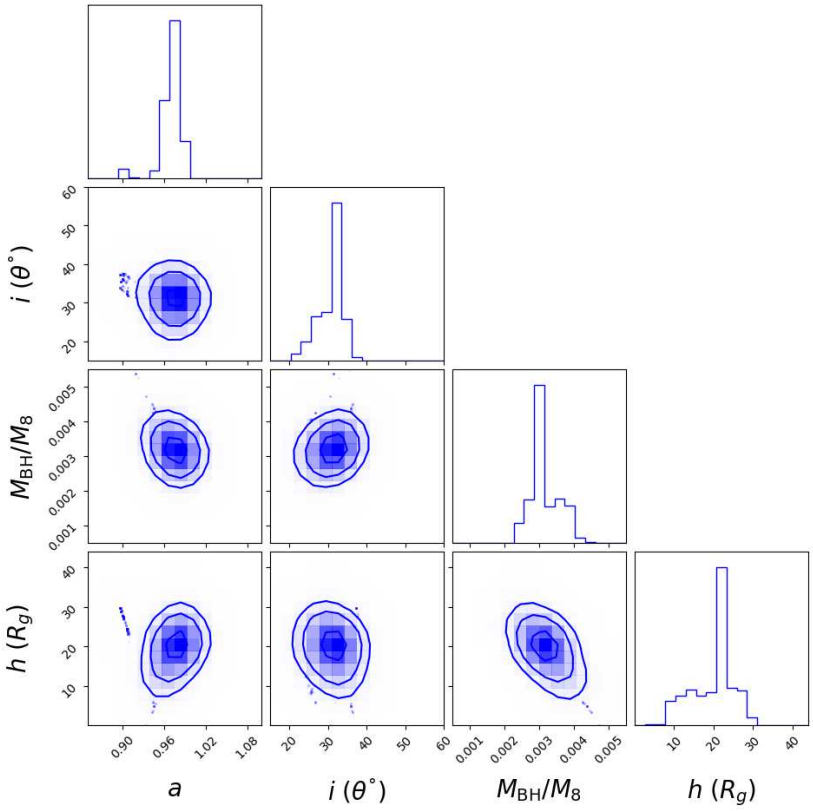
Extended Data Figure 2. *Left:* Lag versus energy spectrum produced from all four epochs (1–4) of the $\sim 116-117$ ks *XMM-Newton* observations (0824610[101-401]). The observations are combined to compute the Fourier time lags from the cross-spectrum, averaging over frequency bins from 0.3 to 6.5×10^{-4} Hz. The lags are obtained between the bands of interest (narrow energy bands, each of width 1 keV) and the 2–10 keV reference band, excluding the bands of interest. The lag spectrum shows a peak lag in the iron-K emission band, with a lag amplitude of 24.80 ± 10 secs. *Right:* Resolving the iron-K profile in the X-ray spectrum. Shown is the representative of the *XMM-Newton* observations from epoch 2, which has a higher signal-to-noise ratio. The data is rebinned for visual clarity.



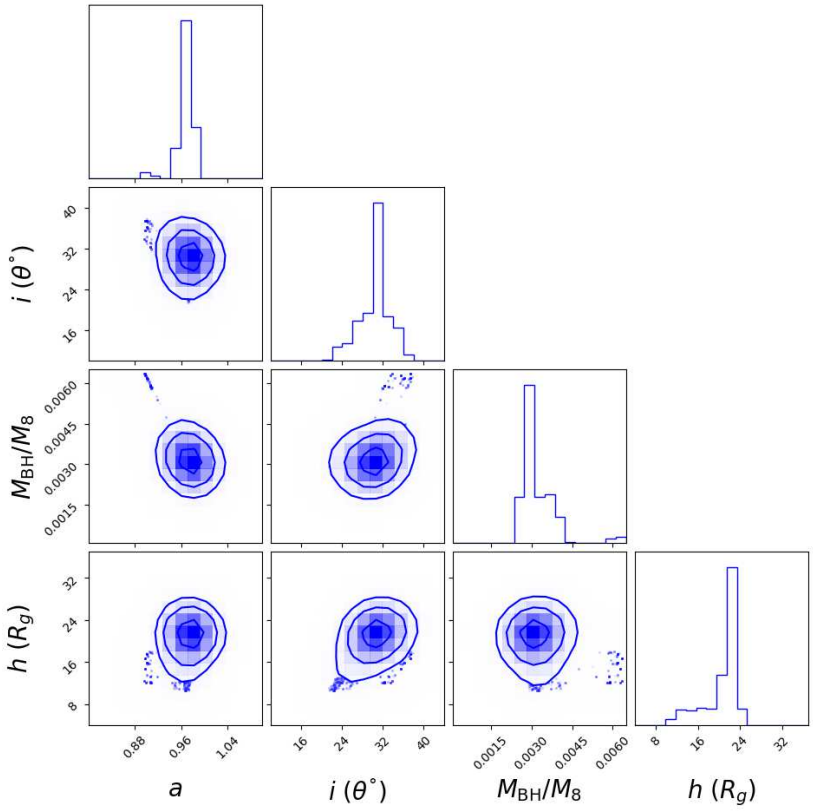
Extended Data Figure 3. Simultaneous fitting of lag-energy spectra of NGC 4395 using the relativistic transfer function model. The best-fit modelled spectra are produced for *XMM-Newton* observations 0824610201 (orange), 0824610301 (black), and the combination of all observations (0824610[101-401]) (blue). The zero lag as a function of energy is shown by the horizontal line (green). The lag-energy spectra are fitted using the relativistic transfer function model KYNREVERB [49]. For model fitting, the number of energy bins is increased to twice the number of energy bins used to observe the iron-K lag (as shown in Figure 2) at the same frequencies, where the average lag amplitude of the 6–7 keV band remains the same. The height h of the corona is allowed to vary freely between the observations, while spin a, black hole mass $M_{\rm BH}$, inclination i, and disc density $n_{\rm d}$ are tied between the observations but allowed to vary freely.



Extended Data Figure 4. MCMC parameters from the relativistic transfer function modelling of the lag-energy spectrum from *XMM-Newton* observation 0824610301. Shown are the corners and posterior distributions of spin a, inclination i, black hole mass $M_{\rm BH}$, and coronal height h derived at 1σ, 2σ, and 3σ confidence. The plot shows that there appears to be no strong degeneracy between the black hole mass and the coronal height.



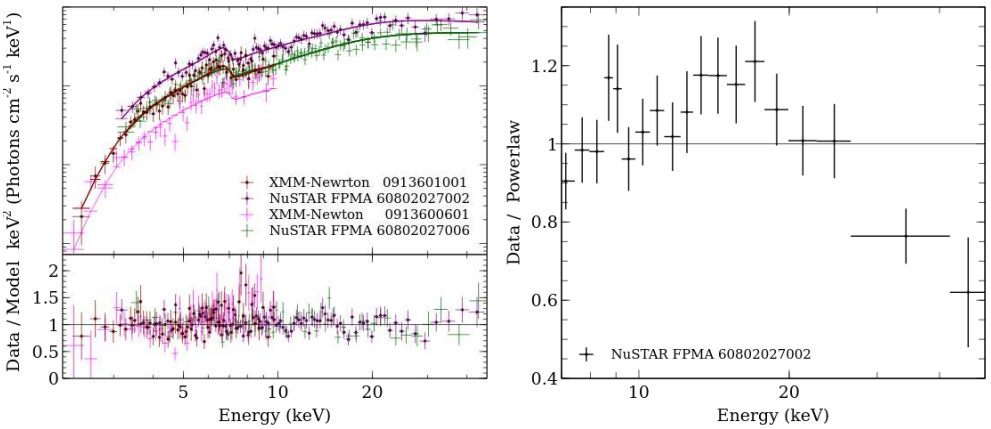
Extended Data Figure 5. MCMC results from the *XMM-Newton* observation 0824610201. The parameters are obtained from the fit of the lag-energy spectrum with the relativistic transfer function model. Corners and posterior distributions are presented for parameters, spin a, inclination i, black hole mass $M_{\rm BH}$, and coronal height h derived at 1σ, 2σ, and 3σ confidence levels. No strong inherent degeneracy appears between the parameters.



Extended Data Figure 6. MCMC results from the reverberation modelling of the combination of all four *XMM-Newton* observations 0824610[101-401]. Corners and posterior distributions are presented for parameters, spin a, inclination i, black hole mass $M_{\rm BH}$, and coronal height h derived at 1σ, 2σ, and 3σ confidence levels. No strong degeneracy appears between the parameters.

Extended Data Table 2. Parameters from the joint transfer function modelling of the lag-energy spectra, computed from all four epochs [1–4] and epochs 2 and 3 of the 2018-2019 *XMM-Newton* observations. The spectra are fitted using the relativistic reflection code KYNREVERB. Parameters from left to right are sequentially 2–10 keV luminosity ($L_{2-10\ \mathrm{keV}}$), coronal height (h), mass of the black hole (M_{BH}), photon index (Γ), disc inclination (i), black hole spin (a), density of the accretion disc (n_{d}), and reduced χ^2_ν per degrees-of-freedom (d.o.f.). Luminosity $L_{2-10\ \mathrm{keV}}$ of all four epochs is estimated from their average. The error bars quoted are at a 1σ confidence.

Obs. ID	$L_{2-10\ \mathrm{keV}}$	h	M_{BH}	Γ	i	a	n_{d}	χ^2_ν/d.o.f.
XMM-Newton	10^{39} erg s^{-1}	$R_{\mathrm{g}}(GM_{\mathrm{BH}}/c^2)$	$10^5\ M_\odot$		degree($\circ$)	Jc/GM_{BH}	10^{15} cm^{-3}	
0824610[101-401]	9.03	$22.67^{+1.83}_{-4.61}$	$3.0^{+3.7}_{-2.8}$	$1.10^{+0.40}_{-0.03}$	$31.50^{+2.77}_{-3.90}$	$0.98^{+0.01}_{-0.02}$	$2.99^{+3.60}_{-0.72}$	35/36
0824610201	8.02	$21.15^{+2.56}_{-3.59}$	–	> 1.05	–	–	–	
0824610301	4.26	$1.65^{+1.86}_{-0.75}$	–	$2.79^{+0.01}_{-0.98}$	–	–	–	



Extended Data Figure 7. *Left: XMM-Newton* and *NuSTAR* spectra of NGC 4395. Best-fit spectra from two different flux epochs are shown as representative of the 2022 observations. The broadband spectra comprising the 2–10 keV *XMM-Newton* band and 3–50 keV *NuSTAR* band are jointly fitted using the relativistic reflection model `relxilllp`. The model concurrently accounts for the observed spectra being due to intrinsic continuum from the corona (described by the powerlaw) and reflection from the disc. *Right:* ratio of *NuSTAR* X-ray spectrum to the best-fitting simple powerlaw model, showing residuals above 10 keV. The curvature-shaped residuals indicate the presence of a Compton hump, arising as a result of reflection from the Compton-thick material.

Extended Data Table 3. Best-fit parameters from the joint spectral modelling of the time-averaged energy spectra from *XMM-Newton* and *NuSTAR* observations obtained in 2022. The spectra are fitted using the relativistic reflection model `relxilllp` in combination with the partially covering absorber component `zxipcf`. Parameters from left to right are sequentially column density ($N_{\rm H}$) of the partially covering absorber, log ionization parameter (ξ) of the partially covering absorber, coronal height (h), high-energy cutoff ($E_{\rm cut}$), photon index (Γ), reflection fraction (R), log ionization parameter (ξ) of the reflection component, 2–10 keV luminosity ($L_{2-10\ \rm keV}$), and reduced χ^2_ν per degrees-of-freedom (d.o.f.). In the analysis, disc inclination is constrained at $\geq 30^\circ$, and the covering fraction of the partially ionized material is found to be < 1. The galactic absorption is fixed at a column density of $N_{\rm H} = 1.85 \times 10^{20}$ cm^{-2} [25]. The quoted error bars are at a 1σ confidence.

Observation ID	$N_{\rm H}^{\rm p}$	$\log\xi^{\rm p}$	h	$E_{\rm cut}$	Γ	R	$\log\xi^{\rm r}$	$L_{2-10\ \rm keV}$	χ^2_ν/d.o.f.
XMM-Newton/*NuSTAR*	10^{22} cm^{-2}	erg cm s^{-1}	$R_{\rm g}$	keV			erg cm s^{-1}	10^{39} erg s^{-1}	
0913601001/60802027002	$8.34^{+0.49}_{-0.36}$	$0.13^{+0.05}_{-0.12}$	$15.55^{+1.52}_{-2.08}$	$60.68^{+8.66}_{-8.04}$	$1.45^{+0.16}_{-0.03}$	$1.77^{+0.16}_{-0.13}$	$1.98^{+0.05}_{-0.13}$	6.56	257/220
0913600101/60802027002	–	–	–	–	–	–	–	–	–
0913600501/60802027004	$9.14^{+1.08}_{-0.70}$	$0.12^{+0.09}_{-0.10}$	$26.66^{+2.71}_{-4.77}$	$54.65^{+9.13}_{-5.63}$	$1.50^{+0.07}_{-0.03}$	$1.10^{+0.38}_{-0.33}$	$1.98^{+0.12}_{-0.50}$	10.16	269/245
0913600601/60802027006	$7.87^{+1.44}_{-0.20}$	$-0.07^{+0.70}_{-0.24}$	$12.50^{+2.66}_{-2.32}$	$59.68^{+8.27}_{-14.9}$	$1.47^{+0.12}_{-0.11}$	$1.63^{+0.35}_{-0.39}$	$2.0^{+0.18}_{-0.50}$	6.03	243/173
0913600701/60802027008	$9.17^{+2.31}_{-0.95}$	$0.85^{+0.20}_{-0.80}$	$19.96^{+7.65}_{-4.03}$	$67.68^{+20.18}_{-3.29}$	$1.40^{+0.20}_{-0.02}$	$0.76^{+0.23}_{-0.15}$	$1.60^{+0.53}_{-0.54}$	7.99	247/210
0913600801/60802027010	$8.38^{+4.53}_{-1.00}$	$0.15^{+0.46}_{-0.32}$	$6.51^{+1.11}_{-1.04}$	$64.37^{+0.84}_{-13.6}$	$1.50^{+0.08}_{-0.07}$	$1.50^{+0.46}_{-0.35}$	< 1.97	4.98	126/129
0913600901/60802027012	$8.36^{+2.20}_{-0.20}$	$0.27^{+0.28}_{-0.14}$	$12.36^{+4.46}_{-0.74}$	$65.22^{+30.0}_{-7.03}$	$1.46^{+0.15}_{-0.05}$	$1.44^{+0.26}_{-0.35}$	$1.70^{+0.40}_{-0.27}$	6.81	175/163

Superscripts p and r represent the corresponding parameters from the partial covering absorber and reflection component, respectively.

References

[1] Uttley, P., Cackett, E.M., Fabian, A.C., Kara, E., Wilkins, D.R.: X-ray reverberation around accreting black holes. **22**, 72 (2014) https://doi.org/10.1007/s00159-014-0072-0 arXiv:1405.6575 [astro-ph.HE]

[2] Emmanoulopoulos, D., Papadakis, I.E., Dovčiak, M., McHardy, I.M.: General relativistic modelling of the negative reverberation X-ray time delays in AGN. **439**(4), 3931–3950 (2014) https://doi.org/10.1093/mnras/stu249 arXiv:1402.0899 [astro-ph.HE]

[3] Reynolds, C.S., Young, A.J., Begelman, M.C., Fabian, A.C.: X-Ray Iron Line Reverberation from Black Hole Accretion Disks. **514**(1), 164–179 (1999) https://doi.org/10.1086/306913 arXiv:astro-ph/9806327 [astro-ph]

[4] Parker, M.L., Wilkins, D.R., Fabian, A.C., Grupe, D., Dauser, T., Matt, G., Harrison, F.A., Brenneman, L., Boggs, S.E., Christensen, F.E., Craig, W.W., Gallo, L.C., Hailey, C.J., Kara, E., Komossa, S., Marinucci, A., Miller, J.M., Risaliti, G., Stern, D., Walton, D.J., Zhang, W.W.: The NuSTAR spectrum of Mrk 335: extreme relativistic effects within two gravitational radii of the event horizon? **443**(2), 1723–1732 (2014) https://doi.org/10.1093/mnras/stu1246 arXiv:1407.8223 [astro-ph.HE]

[5] Wilkins, D.R., Gallo, L.C.: Driving extreme variability: the evolving corona and evidence for jet launching in Markarian 335. **449**(1), 129–146 (2015) https://doi.org/10.1093/mnras/stv162 arXiv:1501.05302 [astro-ph.HE]

[6] Fabian, A.C., Zoghbi, A., Ross, R.R., Uttley, P., Gallo, L.C., Brandt, W.N., Blustin, A.J., Boller, T., Caballero-Garcia, M.D., Larsson, J., Miller, J.M., Miniutti, G., Ponti, G., Reis, R.C., Reynolds, C.S., Tanaka, Y., Young, A.J.: Broad line emission from iron K- and L-shell transitions in the active galaxy 1H0707-495. **459**(7246), 540–542 (2009) https://doi.org/10.1038/nature08007

[7] Zoghbi, A., Fabian, A.C., Reynolds, C.S., Cackett, E.M.: Relativistic iron K X-ray reverberation in NGC 4151. **422**(1), 129–134 (2012) https://doi.org/10.1111/j.1365-2966.2012.20587.x arXiv:1112.1717 [astro-ph.HE]

[8] Cackett, E.M., Fabian, A.C., Zogbhi, A., Kara, E., Reynolds, C., Uttley, P.: A Soft X-Ray Reverberation Lag in the AGN ESO 113-G010. **764**(1), 9 (2013) https://doi.org/10.1088/2041-8205/764/1/L9 arXiv:1210.7874 [astro-ph.HE]

[9] Kara, E., Alston, W.N., Fabian, A.C., Cackett, E.M., Uttley, P., Reynolds, C.S., Zoghbi, A.: A global look at X-ray time lags in Seyfert galaxies. **462**(1), 511–531 (2016) https://doi.org/10.1093/mnras/stw1695 arXiv:1605.02631 [astro-ph.HE]

[10] Uttley, P., Wilkinson, T., Cassatella, P., Wilms, J., Pottschmidt, K., Hanke, M., Böck, M.: The causal connection between disc and power-law variability in hard

state black hole X-ray binaries. **414**(1), 60–64 (2011) https://doi.org/10.1111/j.1745-3933.2011.01056.x arXiv:1104.0634 [astro-ph.HE]

[11] de Marco, B., Ponti, G., Uttley, P., Cappi, M., Dadina, M., Fabian, A.C., Miniutti, G.: PG 1211+143: probing high-frequency lags in a high-mass active galactic nucleus. **417**(1), 98–102 (2011) https://doi.org/10.1111/j.1745-3933.2011.01129.x arXiv:1108.3503 [astro-ph.HE]

[12] Wang, J., Kara, E., Lucchini, M., Ingram, A., van der Klis, M., Mastroserio, G., García, J.A., Dauser, T., Connors, R., Fabian, A.C., Steiner, J.F., Remillard, R.A., Cackett, E.M., Uttley, P., Altamirano, D.: The NICER "Reverberation Machine": A Systematic Study of Time Lags in Black Hole X-Ray Binaries. **930**(1), 18 (2022) https://doi.org/10.3847/1538-4357/ac6262 arXiv:2205.00928 [astro-ph.HE]

[13] Uttley, P., Malzac, J.: Large and complex X-ray time lags from black hole accretion discs with compact inner coronae. **536**(4), 3284–3307 (2025) https://doi.org/10.1093/mnras/stae2514 arXiv:2312.08302 [astro-ph.HE]

[14] Mallick, L., Wilkins, D.R., Alston, W.N., Markowitz, A., De Marco, B., Parker, M.L., Lohfink, A.M., Stalin, C.S.: Discovery of soft and hard X-ray time lags in low-mass AGNs. **503**(3), 3775–3783 (2021) https://doi.org/10.1093/mnras/stab627 arXiv:2101.09594 [astro-ph.HE]

[15] Reynolds, C.S., Nowak, M.A.: Fluorescent iron lines as a probe of astrophysical black hole systems. **377**(6), 389–466 (2003) https://doi.org/10.1016/S0370-1573(02)00584-7 arXiv:astro-ph/0212065 [astro-ph]

[16] Volonteri, M., Madau, P., Quataert, E., Rees, M.J.: The Distribution and Cosmic Evolution of Massive Black Hole Spins. **620**(1), 69–77 (2005) https://doi.org/10.1086/426858 arXiv:astro-ph/0410342 [astro-ph]

[17] Sesana, A., Barausse, E., Dotti, M., Rossi, E.M.: Linking the Spin Evolution of Massive Black Holes to Galaxy Kinematics. **794**(2), 104 (2014) https://doi.org/10.1088/0004-637X/794/2/104 arXiv:1402.7088 [astro-ph.CO]

[18] Fiacconi, D., Sijacki, D., Pringle, J.E.: Galactic nuclei evolution with spinning black holes: method and implementation. **477**(3), 3807–3835 (2018) https://doi.org/10.1093/mnras/sty893 arXiv:1712.00023 [astro-ph.GA]

[19] Greene, J.E., Ho, L.C.: Active Galactic Nuclei with Candidate Intermediate-Mass Black Holes. **610**(2), 722–736 (2004) https://doi.org/10.1086/421719 arXiv:astro-ph/0404110 [astro-ph]

[20] Greene, J.E.: Low-mass black holes as the remnants of primordial black hole formation. Nature Communications **3**, 1304 (2012) https://doi.org/10.1038/ncomms2314 arXiv:1211.7082 [astro-ph.CO]

[21] Volonteri, M., Natarajan, P.: Journey to the M_{BH}-σ relation: the fate of low-mass black holes in the Universe. **400**(4), 1911–1918 (2009) https://doi.org/10.1111/j.1365-2966.2009.15577.x arXiv:0903.2262 [astro-ph.CO]

[22] Kızıltan, B., Baumgardt, H., Loeb, A.: An intermediate-mass black hole in the centre of the globular cluster 47 Tucanae. **542**(7640), 203–205 (2017) https://doi.org/10.1038/nature21361 arXiv:1702.02149 [astro-ph.GA]

[23] Filippenko, A.V., Ho, L.C.: A Low-Mass Central Black Hole in the Bulgeless Seyfert 1 Galaxy NGC 4395. **588**(1), 13–16 (2003) https://doi.org/10.1086/375361 arXiv:astro-ph/0303429 [astro-ph]

[24] Barth, A.J., Ho, L.C., Rutledge, R.E., Sargent, W.L.W.: POX 52: A Dwarf Seyfert 1 Galaxy with an Intermediate-Mass Black Hole. **607**(1), 90–102 (2004) https://doi.org/10.1086/383302 arXiv:astro-ph/0402110 [astro-ph]

[25] Peterson, B.M., Bentz, M.C., Desroches, L.-B., Filippenko, A.V., Ho, L.C., Kaspi, S., Laor, A., Maoz, D., Moran, E.C., Pogge, R.W., Quillen, A.C.: Multiwavelength Monitoring of the Dwarf Seyfert 1 Galaxy NGC 4395. I. A Reverberation-based Measurement of the Black Hole Mass. **632**(2), 799–808 (2005) https://doi.org/10.1086/444494 arXiv:astro-ph/0506665 [astro-ph]

[26] den Brok, M., Seth, A.C., Barth, A.J., Carson, D.J., Neumayer, N., Cappellari, M., Debattista, V.P., Ho, L.C., Hood, C.E., McDermid, R.M.: Measuring the Mass of the Central Black Hole in the Bulgeless Galaxy NGC 4395 from Gas Dynamical Modeling. **809**(1), 101 (2015) https://doi.org/10.1088/0004-637X/809/1/101 arXiv:1507.04358 [astro-ph.GA]

[27] Brum, C., Diniz, M.R., Riffel, R.A., Rodríguez-Ardila, A., Ho, L.C., Riffel, R., Mason, R., Martins, L., Petric, A., Sánchez-Janssen, R.: A close look at the dwarf AGN of NGC 4395: optical and near-IR integral field spectroscopy. **486**(1), 691–707 (2019) https://doi.org/10.1093/mnras/stz893 arXiv:1903.08083 [astro-ph.GA]

[28] Woo, J.-H., Cho, H., Gallo, E., Hodges-Kluck, E., Le, H.A.N., Shin, J., Son, D., Horst, J.C.: A 10,000-solar-mass black hole in the nucleus of a bulgeless dwarf galaxy. Nature Astronomy **3**, 755–759 (2019) https://doi.org/10.1038/s41550-019-0790-3 arXiv:1905.00145 [astro-ph.GA]

[29] McHardy, I.M., Beard, M., Breedt, E., Knapen, J.H., Vincentelli, F.M., Veresvarska, M., Dhillon, V.S., Marsh, T.R., Littlefair, S.P., Horne, K., Glew, R., Goad, M.R., Kammoun, E., Emmanoulopoulos, D.: First detection of the outer edge of an AGN accretion disc: very fast multiband optical variability of NGC 4395 with GTC/HiPERCAM and LT/IO:O. **519**(3), 3366–3382 (2023) https://doi.org/10.1093/mnras/stac3651 arXiv:2212.08015 [astro-ph.GA]

[30] Shih, D.C., Iwasawa, K., Fabian, A.C.: Evidence for an intermediate-mass black

hole and a multi-zone warm absorber in NGC 4395. **341**(3), 973–980 (2003) https://doi.org/10.1046/j.1365-8711.2003.06482.x arXiv:astro-ph/0302108 [astro-ph]

[31] Vaughan, S., Iwasawa, K., Fabian, A.C., Hayashida, K.: The exceptional X-ray variability of the dwarf Seyfert nucleus NGC 4395. **356**(2), 524–530 (2005) https://doi.org/10.1111/j.1365-2966.2004.08463.x arXiv:astro-ph/0410261 [astro-ph]

[32] Dewangan, G.C., Mathur, S., Griffiths, R.E., Rao, A.R.: X-Ray Emission from Active Galactic Nuclei with Intermediate-Mass Black Holes. **689**(2), 762–774 (2008) https://doi.org/10.1086/591728 arXiv:0801.3663 [astro-ph]

[33] Cameron, D.T., McHardy, I., Dwelly, T., Breedt, E., Uttley, P., Lira, P., Arevalo, P.: Correlated X-ray/ultraviolet/optical variability in the very low mass AGN NGC 4395. **422**(1), 902–912 (2012) https://doi.org/10.1111/j.1365-2966.2012.20677.x arXiv:1202.1184 [astro-ph.HE]

[34] McHardy, I.M., Beard, M., Breedt, E., Knapen, J.H., Vincentelli, F.M., Veresvarska, M., Dhillon, V.S., Marsh, T.R., Littlefair, S.P., Horne, K., Glew, R., Goad, M.R., Kammoun, E., Emmanoulopoulos, D.: First detection of the outer edge of an AGN accretion disc: very fast multiband optical variability of NGC 4395 with GTC/HiPERCAM and LT/IO:O. **519**(3), 3366–3382 (2023) https://doi.org/10.1093/mnras/stac3651 arXiv:2212.08015 [astro-ph.GA]

[35] Beard, M.W.J., McHardy, I.M., Horne, K., Cackett, E.M., Vincentelli, F., Hernández Santisteban, J.V., Miller, J., Dhillon, V.S., Knapen, J.H., Littlefair, S.P., Kynoch, D., Breedt, E., Shen, Y., Gelbord, J.: Testing disc reprocessing models for AGN optical variability by comparison of X-ray and optical power spectra of NGC 4395. **537**(1), 293–305 (2025) https://doi.org/10.1093/mnras/staf014 arXiv:2501.02664 [astro-ph.HE]

[36] De Marco, B., Ponti, G., Cappi, M., Dadina, M., Uttley, P., Cackett, E.M., Fabian, A.C., Miniutti, G.: Discovery of a relation between black hole mass and soft X-ray time lags in active galactic nuclei. **431**(3), 2441–2452 (2013) https://doi.org/10.1093/mnras/stt339 arXiv:1201.0196 [astro-ph.HE]

[37] Hancock, S., Young, A.J., Chainakun, P.: X-ray timing and spectral analysis of reverberating active galactic nuclei. **514**(4), 5403–5421 (2022) https://doi.org/10.1093/mnras/stac1653 arXiv:2206.08035 [astro-ph.HE]

[38] Jansen, F., Lumb, D., Altieri, B., Clavel, J., Ehle, M., Erd, C., Gabriel, C., Guainazzi, M., Gondoin, P., Much, R., Munoz, R., Santos, M., Schartel, N., Texier, D., Vacanti, G.: XMM-Newton observatory. I. The spacecraft and operations. **365**, 1–6 (2001) https://doi.org/10.1051/0004-6361:20000036

[39] Harrison, F.A., Craig, W.W., Christensen, F.E., Hailey, C.J., Zhang, W.W., Boggs, S.E., Stern, D., Cook, W.R., Forster, K., Giommi, P., Grefenstette, B.W., Kim, Y., Kitaguchi, T., Koglin, J.E., Madsen, K.K., Mao, P.H., Miyasaka, H.,

Mori, K., Perri, M., Pivovaroff, M.J., Puccetti, S., Rana, V.R., Westergaard, N.J., Willis, J., Zoglauer, A., An, H., Bachetti, M., Barrière, N.M., Bellm, E.C., Bhalerao, V., Brejnholt, N.F., Fuerst, F., Liebe, C.C., Markwardt, C.B., Nynka, M., Vogel, J.K., Walton, D.J., Wik, D.R., Alexander, D.M., Cominsky, L.R., Hornschemeier, A.E., Hornstrup, A., Kaspi, V.M., Madejski, G.M., Matt, G., Molendi, S., Smith, D.M., Tomsick, J.A., Ajello, M., Ballantyne, D.R., Baloković, M., Barret, D., Bauer, F.E., Blandford, R.D., Brandt, W.N., Brenneman, L.W., Chiang, J., Chakrabarty, D., Chenevez, J., Comastri, A., Dufour, F., Elvis, M., Fabian, A.C., Farrah, D., Fryer, C.L., Gotthelf, E.V., Grindlay, J.E., Helfand, D.J., Krivonos, R., Meier, D.L., Miller, J.M., Natalucci, L., Ogle, P., Ofek, E.O., Ptak, A., Reynolds, S.P., Rigby, J.R., Tagliaferri, G., Thorsett, S.E., Treister, E., Urry, C.M.: The Nuclear Spectroscopic Telescope Array (NuSTAR) High-energy X-Ray Mission. **770**(2), 103 (2013) https://doi.org/10.1088/0004-637X/770/2/103 arXiv:1301.7307 [astro-ph.IM]

[40] Gonzalez, A.G., Wilkins, D.R., Gallo, L.C.: Probing the geometry and motion of AGN coronae through accretion disc emissivity profiles. **472**(2), 1932–1945 (2017) https://doi.org/10.1093/mnras/stx2080 arXiv:1708.03205 [astro-ph.HE]

[41] Tanaka, Y., Nandra, K., Fabian, A.C., Inoue, H., Otani, C., Dotani, T., Hayashida, K., Iwasawa, K., Kii, T., Kunieda, H., Makino, F., Matsuoka, M.: Gravitationally redshifted emission implying an accretion disk and massive black hole in the active galaxy MCG-6-30-15. **375**(6533), 659–661 (1995) https://doi.org/10.1038/375659a0

[42] Fabian, A.C., Rees, M.J., Stella, L., White, N.E.: X-ray fluorescence from the inner disc in Cygnus X-1. **238**, 729–736 (1989) https://doi.org/10.1093/mnras/238.3.729

[43] Reynolds, C.S.: Measuring Black Hole Spin Using X-Ray Reflection Spectroscopy. **183**(1-4), 277–294 (2014) https://doi.org/10.1007/s11214-013-0006-6 arXiv:1302.3260 [astro-ph.HE]

[44] Chainakun, P., Young, A.J., Kara, E.: Relativistic X-ray reverberation modelling of the combined time-averaged and lag-energy spectra in AGN. **460**(3), 3076–3088 (2016) https://doi.org/10.1093/mnras/stw1105 arXiv:1605.01300 [astro-ph.HE]

[45] Ingram, A., Mastroserio, G., Dauser, T., Hovenkamp, P., van der Klis, M., García, J.A.: A public relativistic transfer function model for X-ray reverberation mapping of accreting black holes. **488**(1), 324–347 (2019) https://doi.org/10.1093/mnras/stz1720 arXiv:1906.08310 [astro-ph.HE]

[46] Chiang, C.-Y., Fabian, A.C.: Modelling the broad-band spectra of MCG-6-30-15 with a relativistic reflection model. **414**(3), 2345–2353 (2011) https://doi.org/10.1111/j.1365-2966.2011.18553.x arXiv:1104.4483 [astro-ph.HE]

[47] Walton, D.J., Zoghbi, A., Cackett, E.M., Uttley, P., Harrison, F.A., Fabian, A.C., Kara, E., Miller, J.M., Reis, R.C., Reynolds, C.S.: Hard X-Ray Lags in Active Galactic Nuclei: Testing the Distant Reverberation Hypothesis with NGC 6814. **777**(2), 23 (2013) https://doi.org/10.1088/2041-8205/777/2/L23 arXiv:1310.0822 [astro-ph.HE]

[48] De Marco, B., Ponti, G., Muñoz-Darias, T., Nandra, K.: Tracing the Reverberation Lag in the Hard State of Black Hole X-Ray Binaries. **814**(1), 50 (2015) https://doi.org/10.1088/0004-637X/814/1/50 arXiv:1510.02798 [astro-ph.HE]

[49] Caballero-García, M.D., Papadakis, I.E., Dovčiak, M., Bursa, M., Epitropakis, A., Karas, V., Svoboda, J.: Testing the X-ray reverberation model KYNREFREV in a sample of Seyfert 1 Active Galactic Nuclei. **480**(2), 2650–2659 (2018) https://doi.org/10.1093/mnras/sty1990 arXiv:1804.03503 [astro-ph.HE]

[50] Fabian, A.C., Lohfink, A., Kara, E., Parker, M.L., Vasudevan, R., Reynolds, C.S.: Properties of AGN coronae in the NuSTAR era. **451**(4), 4375–4383 (2015) https://doi.org/10.1093/mnras/stv1218 arXiv:1505.07603 [astro-ph.HE]

[51] García, J., Dauser, T., Lohfink, A., Kallman, T., Steiner, J., McClintock, J., Brenneman, L., Wilms, J., Eikmann, W., Reynolds, C., *et al.*: Improved reflection models of black hole accretion disks: treating the angular distribution of x-rays. The Astrophysical Journal **782**(2), 76 (2014)

[52] Dauser, T., Garcia, J., Parker, M.L., Fabian, A.C., Wilms, J.: The role of the reflection fraction in constraining black hole spin. **444**, 100–104 (2014) https://doi.org/10.1093/mnrasl/slu125 arXiv:1408.2347 [astro-ph.HE]

[53] García, J.A., Dauser, T., Steiner, J.F., McClintock, J.E., Keck, M.L., Wilms, J.: On Estimating the High-energy Cutoff in the X-Ray Spectra of Black Holes via Reflection Spectroscopy. **808**(2), 37 (2015) https://doi.org/10.1088/2041-8205/808/2/L37 arXiv:1505.03616 [astro-ph.HE]

[54] García, J.A., Dauser, T., Ludlam, R., Parker, M., Fabian, A., Harrison, F.A., Wilms, J.: Relativistic X-Ray Reflection Models for Accreting Neutron Stars. **926**(1), 13 (2022) https://doi.org/10.3847/1538-4357/ac3cb7 arXiv:2111.12838 [astro-ph.HE]

[55] Kara, E., García, J.A., Lohfink, A., Fabian, A.C., Reynolds, C.S., Tombesi, F., Wilkins, D.R.: The high-Eddington NLS1 Ark 564 has the coolest corona. **468**(3), 3489–3498 (2017) https://doi.org/10.1093/mnras/stx792 arXiv:1703.09815 [astro-ph.HE]

[56] Guilbert, P.W., Fabian, A.C., Rees, M.J.: Spectral and variability constraints on compact sources. **205**, 593–603 (1983) https://doi.org/10.1093/mnras/205.3.593

[57] Cho, H., Woo, J.-H., Hodges-Kluck, E., Son, D., Shin, J., Gallo, E., Bae, H.-J., Brink, T.G., Cho, W., Filippenko, A.V., Horst, J.C., Ilić, D., Joner, M.D., Kang, D., Kang, W., Kaspi, S., Kim, T., Kovačević, A.B., Kumar, S., Le, H.A.N., Nadzhip, A.E., Pozo Nuñez, F., Metlov, V.G., Oknyansky, V.L., Park, S., Popović, L.č., Rakshit, S., Schramm, M., Shatsky, N.I., Spencer, M., Sung, E.-C., Sung, H.-i., Tatarnikov, A.M., Vince, O.: Variability and the Size-Luminosity Relation of the Intermediate-mass AGN in NGC 4395. **892**(2), 93 (2020) https://doi.org/10.3847/1538-4357/ab7a98 arXiv:2002.08028 [astro-ph.GA]

[58] Svensson, R.: Steady mildly relativistic thermal plasmas - Processes and properties. **209**, 175–208 (1984) https://doi.org/10.1093/mnras/209.2.175

[59] Zdziarski, A.A.: Power-law X-ray and gamma-ray emission from relativistic thermal plasmas. **289**, 514–525 (1985) https://doi.org/10.1086/162912

[60] Gallo, L.: X-ray perspective of Narrow-line Seyfert 1 galaxies. In: Revisiting Narrow-Line Seyfert 1 Galaxies and Their Place in the Universe, p. 34 (2018). https://doi.org/10.22323/1.328.0034

[61] Alston, W.N., Fabian, A.C., Kara, E., Parker, M.L., Dovciak, M., Pinto, C., Jiang, J., Middleton, M.J., Miniutti, G., Walton, D.J., Wilkins, D.R., Buisson, D.J.K., Caballero-Garcia, M.D., Cackett, E.M., De Marco, B., Gallo, L.C., Lohfink, A.M., Reynolds, C.S., Uttley, P., Young, A.J., Zogbhi, A.: A dynamic black hole corona in an active galaxy through X-ray reverberation mapping. Nature Astronomy **4**, 597–602 (2020) https://doi.org/10.1038/s41550-019-1002-x arXiv:2001.06454 [astro-ph.HE]

[62] Reynolds, C.S.: Observing black holes spin. Nature Astronomy **3**, 41–47 (2019) https://doi.org/10.1038/s41550-018-0665-z arXiv:1903.11704 [astro-ph.HE]

[63] Vasudevan, R.V., Fabian, A.C., Reynolds, C.S., Aird, J., Dauser, T., Gallo, L.C.: A selection effect boosting the contribution from rapidly spinning black holes to the cosmic X-ray background. **458**(2), 2012–2023 (2016) https://doi.org/10.1093/mnras/stw363 arXiv:1506.01027 [astro-ph.HE]

[64] Wilkins, D.R., Gallo, L.C., Costantini, E., Brandt, W.N., Blandford, R.D.: Light bending and X-ray echoes from behind a supermassive black hole. **595**(7869), 657–660 (2021) https://doi.org/10.1038/s41586-021-03667-0 arXiv:2107.13555 [astro-ph.HE]

[65] García, J.A., Fabian, A.C., Kallman, T.R., Dauser, T., Parker, M.L., McClintock, J.E., Steiner, J.F., Wilms, J.: The effects of high density on the X-ray spectrum reflected from accretion discs around black holes. **462**(1), 751–760 (2016) https://doi.org/10.1093/mnras/stw1696 arXiv:1603.05259 [astro-ph.HE]

[66] Kara, E., Steiner, J.F., Fabian, A.C., Cackett, E.M., Uttley, P., Remillard, R.A., Gendreau, K.C., Arzoumanian, Z., Altamirano, D., Eikenberry, S., Enoto, T.,

Homan, J., Neilsen, J., Stevens, A.L.: The corona contracts in a black-hole transient. **565**(7738), 198–201 (2019) https://doi.org/10.1038/s41586-018-0803-x arXiv:1901.03877 [astro-ph.HE]

[67] Walton, D.J., Brightman, M., Risaliti, G., Fabian, A.C., Fürst, F., Harrison, F.A., Lohfink, A., Matt, G., Miniutti, G., Parker, M.L., Stern, D.: Disentangling the complex broad-band X-ray spectrum of IRAS 13197-1627 with NuSTAR, XMM-Newton and Suzaku. **473**(4), 4377–4391 (2018) https://doi.org/10.1093/mnras/stx2659 arXiv:1706.02088 [astro-ph.HE]

[68] Sun, S., Guainazzi, M., Ni, Q., Wang, J., Qian, C., Shi, F., Wang, Y., Bambi, C.: Multi-epoch analysis of the X-ray spectrum of the active galactic nucleus in NGC 5506. **478**(2), 1900–1910 (2018) https://doi.org/10.1093/mnras/sty1233 arXiv:1704.03716 [astro-ph.HE]

[69] Xu, Y., Baloković, M., Walton, D.J., Harrison, F.A., García, J.A., Koss, M.J.: Evidence for Relativistic Disk Reflection in the Seyfert 1h Galaxy/ULIRG IRAS 05189-2524 Observed by NuSTAR and XMM-Newton. **837**(1), 21 (2017) https://doi.org/10.3847/1538-4357/aa5df4 arXiv:1702.00073 [astro-ph.HE]

[70] Nowak, M.A., Vaughan, B.A., Wilms, J., Dove, J.B., Begelman, M.C.: Rossi X-Ray Timing Explorer Observation of Cygnus X-1. II. Timing Analysis. **510**(2), 874–891 (1999) https://doi.org/10.1086/306610 arXiv:astro-ph/9807278 [astro-ph]

[71] Kara, E., Fabian, A.C., Cackett, E.M., Miniutti, G., Uttley, P.: Revealing the X-ray source in IRAS 13224-3809 through flux-dependent reverberation lags. **430**(2), 1408–1413 (2013) https://doi.org/10.1093/mnras/stt024 arXiv:1301.1924 [astro-ph.HE]

[72] Miller, L., Turner, T.J., Reeves, J.N., Braito, V.: X-ray reverberation in 1H0707-495 revisited. **408**(3), 1928–1935 (2010) https://doi.org/10.1111/j.1365-2966.2010.17261.x arXiv:1006.5035 [astro-ph.HE]

[73] Zoghbi, A., Uttley, P., Fabian, A.C.: Understanding reverberation lags in 1H0707-495. **412**(1), 59–64 (2011) https://doi.org/10.1111/j.1365-2966.2010.17883.x arXiv:1010.3744 [astro-ph.HE]

[74] Kara, E., Fabian, A.C., Marinucci, A., Matt, G., Parker, M.L., Alston, W., Brenneman, L.W., Cackett, E.M., Miniutti, G.: The changing X-ray time lag in MCG-6-30-15. **445**(1), 56–65 (2014) https://doi.org/10.1093/mnras/stu1750 arXiv:1408.5051 [astro-ph.HE]

[75] Zoghbi, A., Miller, J.M., Cackett, E.: Revisiting the Spectral and Timing Properties of NGC 4151. **884**(1), 26 (2019) https://doi.org/10.3847/1538-4357/ab3e31 arXiv:1908.09862 [astro-ph.HE]

[76] Zoghbi, A., Kalli, S., Miller, J.M., Mizumoto, M.: Testing the Lamp-post and Wind Reverberation Models with XMM-Newton Observations of NGC 5506. **893**(2), 97 (2020) https://doi.org/10.3847/1538-4357/ab7dc8 arXiv:2003.04322 [astro-ph.HE]

[77] Miniutti, G., Fabian, A.C.: A light bending model for the X-ray temporal and spectral properties of accreting black holes. **349**(4), 1435–1448 (2004) https://doi.org/10.1111/j.1365-2966.2004.07611.x arXiv:astro-ph/0309064 [astro-ph]

[78] Wilkins, D.R., Fabian, A.C.: The origin of the lag spectra observed in AGN: Reverberation and the propagation of X-ray source fluctuations. **430**(1), 247–258 (2013) https://doi.org/10.1093/mnras/sts591 arXiv:1212.2213 [astro-ph.HE]

[79] Arnaud, K.A.: XSPEC: The First Ten Years. In: Jacoby, G.H., Barnes, J. (eds.) Astronomical Data Analysis Software and Systems V. Astronomical Society of the Pacific Conference Series, vol. 101, p. 17 (1996)

[80] García, J., Dauser, T., Reynolds, C.S., Kallman, T.R., McClintock, J.E., Wilms, J., Eikmann, W.: X-Ray Reflected Spectra from Accretion Disk Models. III. A Complete Grid of Ionized Reflection Calculations. **768**(2), 146 (2013) https://doi.org/10.1088/0004-637X/768/2/146 arXiv:1303.2112 [astro-ph.HE]

[81] Dauser, T., Garcia, J., Wilms, J., Böck, M., Brenneman, L.W., Falanga, M., Fukumura, K., Reynolds, C.S.: Irradiation of an accretion disc by a jet: general properties and implications for spin measurements of black holes. **430**(3), 1694–1708 (2013) https://doi.org/10.1093/mnras/sts710 arXiv:1301.4922 [astro-ph.HE]

[82] Reeves, J., Done, C., Pounds, K., Terashima, Y., Hayashida, K., Anabuki, N., Uchino, M., Turner, M.: On why the iron K-shell absorption in AGN is not a signature of the local warm/hot intergalactic medium. **385**(1), 108–112 (2008) https://doi.org/10.1111/j.1745-3933.2008.00443.x arXiv:0801.1587 [astro-ph]

[83] Wilms, J., Allen, A., McCray, R.: On the Absorption of X-Rays in the Interstellar Medium. **542**(2), 914–924 (2000) https://doi.org/10.1086/317016 arXiv:astro-ph/0008425 [astro-ph]

[84] Ghosh, T., Rana, V., Bachetti, M.: Hard X-Ray Flares and Spectral Variability in NGC 4395 ULX1. **938**(1), 76 (2022) https://doi.org/10.3847/1538-4357/ac8f8f arXiv:2202.01432 [astro-ph.HE]

[85] Done, C., Davis, S.W., Jin, C., Blaes, O., Ward, M.: Intrinsic disc emission and the soft X-ray excess in active galactic nuclei. **420**(3), 1848–1860 (2012) https://doi.org/10.1111/j.1365-2966.2011.19779.x arXiv:1107.5429 [astro-ph.HE]